SPECIAL
Climate and Frontal Air-Sea Interaction
COLLECTION

Interannual Modulations of Oceanic Imprints on the Wintertime Atmospheric Boundary Layer under the Changing Dynamical Regimes of the Kuroshio Extension

RYUSUKE MASUNAGA

Research Center for Advanced Science and Technology, The University of Tokyo, Tokyo, Japan

HISASHI NAKAMURA

Research Center for Advanced Science and Technology, The University of Tokyo, Tokyo, Japan, and Application Laboratory, Japan Agency for Marine-Earth Science and Technology, Yokohama, Japan

TAKAFUMI MIYASAKA AND KAZUAKI NISHII

Research Center for Advanced Science and Technology, The University of Tokyo, Tokyo, Japan

BO QIU

Department of Oceanography, University of Hawai'i at Mānoa, Honolulu, Hawaii

(Manuscript received 5 August 2015, in final form 9 January 2016)

ABSTRACT

The Kuroshio Extension (KE) fluctuates between its different dynamic regimes on (quasi) decadal time scales. In its stable (unstable) regime, the KE jet is strengthened (weakened) and less (more) meandering. The present study investigates wintertime mesoscale atmospheric structures modulated under the changing KE regimes, as revealed in high-resolution satellite data and data from a particular atmospheric reanalysis (ERA-Interim). In the unstable KE regime, a positive anomaly in sea surface temperature (SST) to the north of the climatological KE jet accompanies positive anomalies in upward heat fluxes from the ocean, surface wind convergence, and cloudiness. As revealed in the atmospheric reanalysis, these positive anomalies coincide with local lowering of sea level pressure, weaker vertical wind shear, warming and thickening of the marine atmospheric boundary layer (MABL), anomalous ascent, and convective precipitation. In the stable KE regime, by contrast, the corresponding imprints of sharp SST gradients across the KE and Oyashio fronts on the wintertime MABL are separated more distinctly, and so are the surface baroclinic zones along those two SST fronts. In the ERA-Interim data, such mesoscale imprints of the KE variability as above are not well represented in a period during which the resolution of SST data prescribed is relatively low. The present study thus elucidates the importance of high-resolution SST data prescribed for atmospheric reanalysis in representing modulations of the MABL structure and air–sea fluxes by the variability of oceanic fronts and/or jets, including the modulations occurring with the changing KE regimes through the hydrostatic pressure adjustment and vertical mixing mechanisms.

1. Introduction

In the Kuroshio–Oyashio Extension (KOE) region, also known as the subarctic oceanic frontal zone (SAFZ), part of the cool Oyashio water flows southward along the east coast of Japan to strengthen the sea surface temperature (SST) gradient locally on the northern

Denotes Open Access content.

Corresponding author address: Ryusuke Masunaga, Research Center for Advanced Science and Technology, The University of Tokyo, 4-6-1 Komaba, Meguro-ku, Tokyo, 153-8904, Japan.
E-mail: masunaga@atmos.rcast.u-tokyo.ac.jp

DOI: 10.1175/JCLI-D-15-0545.1

flank of the warm Kuroshio Extension (KE), while the rest flows eastward to the north of the KE, forming the mixed water region in between (Kawai 1972; Yasuda 2003; Kida et al. 2015). Within the wintertime KOE region, turbulent sensible heat flux (SHF) and latent heat flux (LHF) from the ocean surface are enhanced into a cool dry continental air mass carried by the prevailing monsoonal northerlies (e.g., Kwon et al. 2010), especially along the KE because of locally augmented air–sea temperature differences (e.g., Taguchi et al. 2009; Tanimoto et al. 2011). It has been argued that sharp meridional contrasts in SHF across SST fronts act to restore near-surface baroclinicity efficiently, contributing to the recurrent development of synoptic-scale disturbances along the Pacific storm track (Nakamura et al. 2004, 2008; Taguchi et al. 2009; Sampe et al. 2010; Hotta and Nakamura 2011).

The SAFZ is recognized as one of the major centers of action of decadal SST variability within the Pacific basin (Nakamura et al. 1997). The meridional displacement of the frontal axis yields persistent SST anomalies (Seager et al. 2001; Nakamura and Kazmin 2003; Nonaka et al. 2006), in modifying SHF and LHF into the overlying atmosphere (Tanimoto et al. 2003; Taguchi et al. 2012). As shown recently, the decadal SST anomalies in the KOE region can significantly modify the basin-scale atmospheric circulation by modulating storm-track activity (Frankignoul et al. 2011; Taguchi et al. 2012; Smirnov et al. 2015).

Recent studies have revealed that locally enhanced turbulent heat fluxes due to warm SST can organize mesoscale structures in the marine atmospheric boundary layer (MABL) that cannot form only through atmospheric processes (e.g., Xie 2004; Small et al. 2008; Kelly et al. 2010). Locally warm SST can reduce static stability within the overlying MABL, where the ''vertical mixing effect'' enhances downward transport of wind momentum to locally accelerate surface winds (Wallace et al. 1989; Hayes et al. 1989), leading to positive local correlation between surface wind speed and SST (Nonaka and Xie 2003). Mesoscale SST distribution in oceanic frontal zones can therefore induce surface wind convergence or divergence (e.g., Chelton et al. 2004; O'Neill et al. 2010). At the same time, local SST maxima and minima modulate heat fluxes into the overlying atmosphere, leading to the formation of local minima and maxima, respectively, of sea level pressure (SLP) through ''hydrostatic effect'' (Lindzen and Nigam 1987). This process is ubiquitously operative over SST frontal regions (Shimada and Minobe 2011). Actually, the wintertime climatology based on in situ observations shows a distinct SLP trough along the KE (Tanimoto et al. 2011). Enhanced surface wind convergence due to the vertical mixing effect and/or hydrostatic effect can locally strengthen upward motion, which can reach the midtroposphere in many occasions, enhancing cloud formation and precipitation (Minobe et al. 2008, 2010; Tokinaga et al. 2009; Frenger et al. 2013; Masunaga et al. 2015).

Westward-propagating wind-forced oceanic Rossby waves are shown to play an important role in determining the sea surface height (SSH) field in the vicinity of the KE and thus modulating its path and eastward transport (Schneider et al. 2002; Qiu 2003; Nonaka et al. 2006; Taguchi et al. 2007; Qiu and Chen 2010; Sasaki et al. 2013; Qiu et al. 2014). It has been pointed out that the KE fluctuates between its stable and unstable regimes on (quasi) decadal time scales (e.g., Qiu and Chen 2005). In its unstable regime, eastward transport of the KE decreases, and its path tends to be more meandering, compared to its stable regime. From the unstable KE jet, more warm-core oceanic eddies are pinched off northward, leading to higher SST and enhanced upward SHF and LHF to the north of the mean KE path (Sugimoto and Hanawa 2011; Sasaki and Minobe 2015). Iizuka (2010) indicated through regional atmospheric model simulations that the warm SST anomaly can enhance winter precipitation, and its imprints can reach the free troposphere. Using their own measures of the KE regimes derived from SSH and/or SST fields, several studies have documented relationship between the KE variability and large-scale atmospheric circulation, including the strength of the Aleutian low and storm-track activity (Seo et al. 2014; Qiu et al. 2014; O'Reilly and Czaja 2015; Révelard et al. 2016).

This paper aims at a comprehensive investigation of interannual variability in wintertime mesoscale atmospheric features associated with the KE variability based on the particular index updated by Qiu et al. (2014). We take advantage of high-resolution state-of-the-art satellite measurements available in this century in addition to the ERA-Interim global atmospheric reanalysis (Dee et al. 2011), for which the resolution of the SST data prescribed became high enough since 2002 to resolve frontal signatures. It has been shown that the representation of mesoscale SST features is crucial for representing mesoscale features in surface winds (Chelton 2005; Song et al. 2009), cloudiness, and precipitation (Masunaga et al. 2015) in global reanalysis data. Our primary focus is therefore on the KE variability in this century. The present study can be complementary to Wang and Liu (2016), who investigated the local response of mesoscale atmospheric fields to the KE variability using their own KE index.

The rest of this paper is organized as follows. The datasets used in the present study are introduced in section 2. In sections 3, we investigate interannual variability of wintertime SST and associated mesoscale atmospheric variability based on satellite-based data through composite analysis. In section 4, a similar analysis is applied to the ERA-Interim, with particular emphasis on mesoscale

vertical structure of the MABL. In section 5, we explore dominant factors in determining heat flux anomalies through linearized bulk aerodynamic formulas. In section 6, influence of the KE variability on surface baroclinic zones is examined through a composite analysis applied to a frontogenetical function. A summary and concluding remarks are given in section 7.

2. Data

a. Satellite-based observational data

For SST, the Advanced Very High Resolution Radiometer (AVHRR) Pathfinder Optimum Interpolation SST (OISST) dataset produced by the National Oceanic and Atmospheric Administration (NOAA) is used (Reynolds et al. 2007). The monthly data are available since November 1981 on a 0.25° × 0.25° latitude–longitude grid. This resolution is high enough to represent mesoscale SST variability associated with the KE regime changes.

Monthly mean sea surface wind velocities are derived from the National Aeronautics and Space Administration's (NASA) Quick Scatterometer (QuikSCAT) measurements (Perry 2001). The data are available originally on a 0.25° × 0.25° grid from September 1999 to October 2009. Monthly mean precipitation data used are based on the Advanced Microwave Scanning Radiometer for Earth Observing System (AMSR-E) (Wentz et al. 2014), available on a 0.25° × 0.25° grid from June 2002 to September 2011. The monthly mean fields of wind velocities and precipitation have been interpolated onto the same 0.75° × 0.75° grid system as for the ERA-Interim to suppress small-scale noises before computing divergence or meridional high-pass filtering.

Monthly cloudiness is based on the Moderate Resolution Imaging Spectroradiometer (MODIS) collection 051 level-3 product (Hubanks et al. 2008). The MODIS instrument has been on board NASA satellites *Terra* and *Aqua*. The product is available on a 1.0° × 1.0° grid for the period from July 2002 to August 2012.

Objectively analyzed air–sea fluxes (OAFlux) are used for monthly mean fluxes of sensible and latent heat at the sea surface (Yu et al. 2008), available on a 1.0° × 1.0° grid since January 1958. The data are constructed through the COARE 3.0 flux algorithm (Fairall et al. 2003) from data measured by several satellites, including OISST and wind products derived from AMSR-E and QuikSCAT and atmospheric reanalysis outputs of the National Centers for Environmental Prediction–National Center for Atmospheric Research (NCEP–NCAR) reanalysis (Kalnay et al. 1996; Kanamitsu et al. 2002) and the 40-yr European Centre for Medium-Range Weather Forecasts Re-Analysis (ERA-40; Uppala et al. 2005). Daily mean SST, surface air temperature (SAT), surface specific humidity, and surface wind speed are also used, which are available from 1985.

b. ERA-Interim

Since some atmospheric variables (e.g., SLP) and detailed vertical structures of the atmospheric boundary layer are difficult to measure from satellites, global atmospheric reanalysis data from ERA-Interim are also utilized (Dee et al. 2011). The data are available from January 1979 on a 0.75° × 0.75° grid, which is fine enough to represents mesoscale atmospheric structures. We use monthly and 6-hourly fields of three-dimensional atmospheric motion, SLP, geopotential height, temperature, and humidity, available at pressure levels at intervals of 25 hPa below the 750-hPa level. In addition, the boundary layer height, cloud amount, and convective and large-scale precipitation are used. As surface winds, we use wind velocities at the lowest model level rather than 10-m winds, which depend strongly on MABL parameterization schemes. We have confirmed that both wind velocities yield virtually the same results. In the same manner, variables at the lowest model level are considered as their surface fields (e.g., SAT). We also use SHF and LHF at the ocean surface as outputs from the forecasting system.

As documented by Masunaga et al. (2015) in detail, the resolution of prescribed SST for the ERA-Interim has been improved since January 2002. The KE and Oyashio fronts and associated mesoscale atmospheric distributions are properly represented in the wintertime climatologies constructed for the period from 2002 to 2012, while they are missing in the earlier period for which the resolution of the SST data is substantially lower. In the present study, the period from 2002 to 2014 is referred to as a high-resolution (HR) SST period and the earlier period as a low-resolution (LR) SST period.

3. Interannual variability of SST and its imprints on the overlying MABL based on the satellite-based observational data

a. The KE index and mesoscale SST variability

In Fig. 1a, winter-mean (December–March) time series of the KE index (KEI) defined by Qiu et al. (2014) is plotted with a black line. The index has been constructed as weekly SSH anomalies averaged within 31°–36°N, 140°–165°E. This domain encompasses the KE jet and its southern recirculation gyre, whose strength is closely tied to their decadal modulations. Since satellite altimeter data are not available until

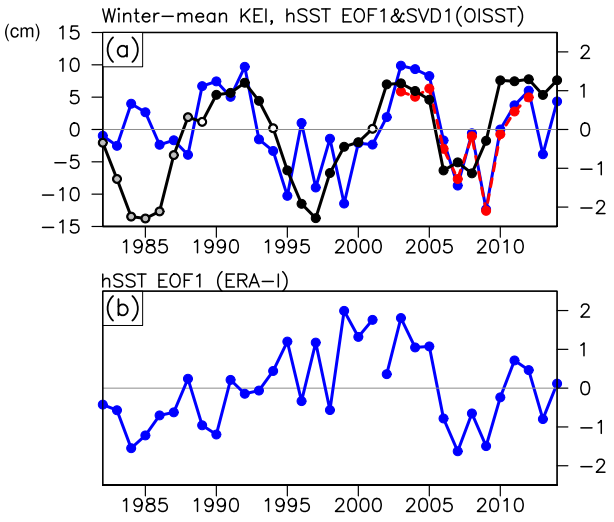

FIG. 1. (a) Winter-mean KEI (black line) (cm; left *y* axis) defined by Qiu et al. (2014). Positive and negative values correspond to the stable and unstable regimes, respectively, of the KE. Gray-filled circles signify winters in 1982–88, which are excluded from our entire analysis. Open circles signify near-normal winters, for each of which the absolute value of the index is less than 25% of its std dev for 1989–2014 (6.4 cm), and those winters are excluded from our composite analysis. The blue line indicates the normalized leading PC time series (right *y* axis) of winter-mean anomalies in hSST over the KOE region (32.875°–41.875°N, 142.125°–149.875°E; gray box in Fig. 2a) based on OISST. The red line shows the time series of the hSST variability (right *y* axis) defined as its leading SVD mode with MODIS hTCA over 32.5°–41.5°N, 141.5°–149.5°E (gray box in Fig. 2b). (b) As in (a), but for the leading PC time series of hSST (blue lines) based on the ERA-Interim evaluated for 1982–2001 and 2002–14, separately.

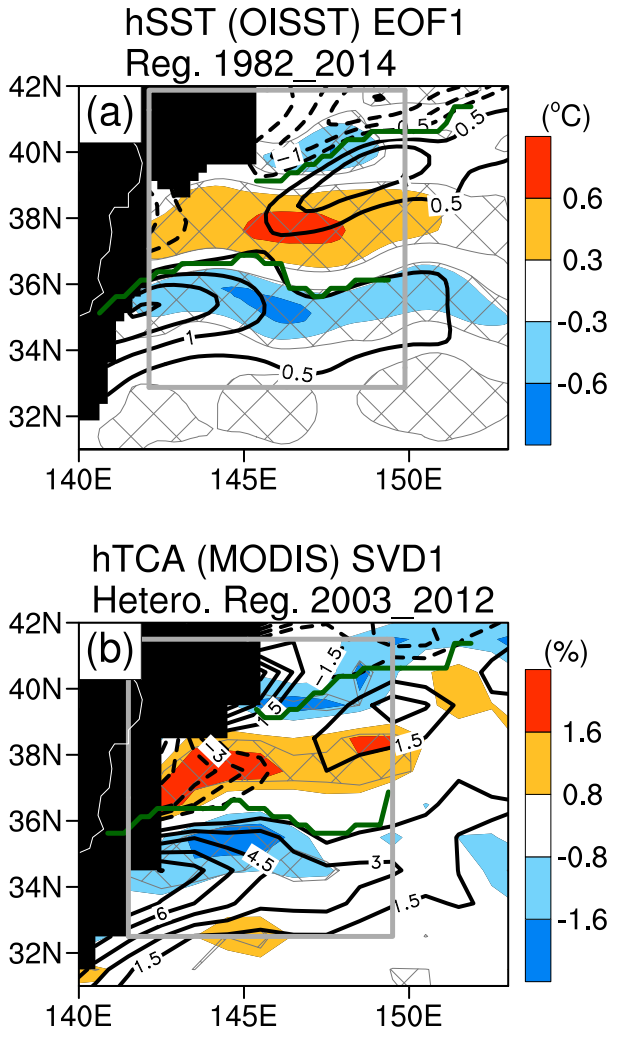

FIG. 2. (a) Wintertime (December–March) anomalies of hSST (°C; shaded) regressed linearly onto its leading PC time series (blue line in Fig. 1a; defined for a domain indicated by gray rectangle) and its wintertime climatology (contoured every 0.5°C; dashed for negative; zero lines are omitted) for the period 1982–2014, representing typical anomaly patterns observed when the reference time series are negative. Gray hatched areas are overlaid where local correlation with the time series is statistically significant at the 90% confidence level. Green lines indicate the axes of the KE and Oyashio fronts at which climatological-mean equatorward SST gradients maximize locally for the period. (b) Same as in (a), but for anomalies of hTCA (%; shaded) regressed linearly onto the wintertime hSST variability derived as its leading SVD (red line in Fig. 1a) (i.e., heterogeneous regression map) and its wintertime climatology (contoured every 1.5%; dashed for negative; zero contours are omitted) for the period 2003–12.

October 1992 (Ducet et al. 2000), for the index for the earlier period the SSH output from a hindcast run of the OGCM for the Earth Simulator (OFES; Sasaki et al. 2008) has been merged. The positive index, for example, is represented in the stable regime of the KE, characterized by enhanced surface current transport and straight path of the KE jet. Plotted with the KEI is the normalized principal component (PC) time series for the leading EOF of meridionally high-pass-filtered SST (blue line) for the KOE region (32.875°–41.875°N, 142.125°–149.875°E; gray box in Fig. 2a), which explains 26% of the total variance of OISST over the region. A meridional high-pass filter, defined as local departures from meridional 27-point (equivalent to 6.75° latitudinal width) running-mean values, has been applied to highlight mesoscale SST features (denoted as hSST). Note that the leading EOF of hSST based on the OFES hindcast output is similar to its observational counterpart, and neither of them is particularly sensitive to slight modifications in the analysis domain and period. In the unstable KE regime when the leading PC time series is negative (Fig. 2a), a typical anomaly pattern of hSST is characterized by zonally elongated dipolar anomalies with warming to the north of the mean KE jet marked as a belt of local hSST maxima in its wintertime climatology (contours in Fig. 2a). Except in the mid-1980s, KEI overall captures decadal-scale SST variability associated with the leading EOF. In the

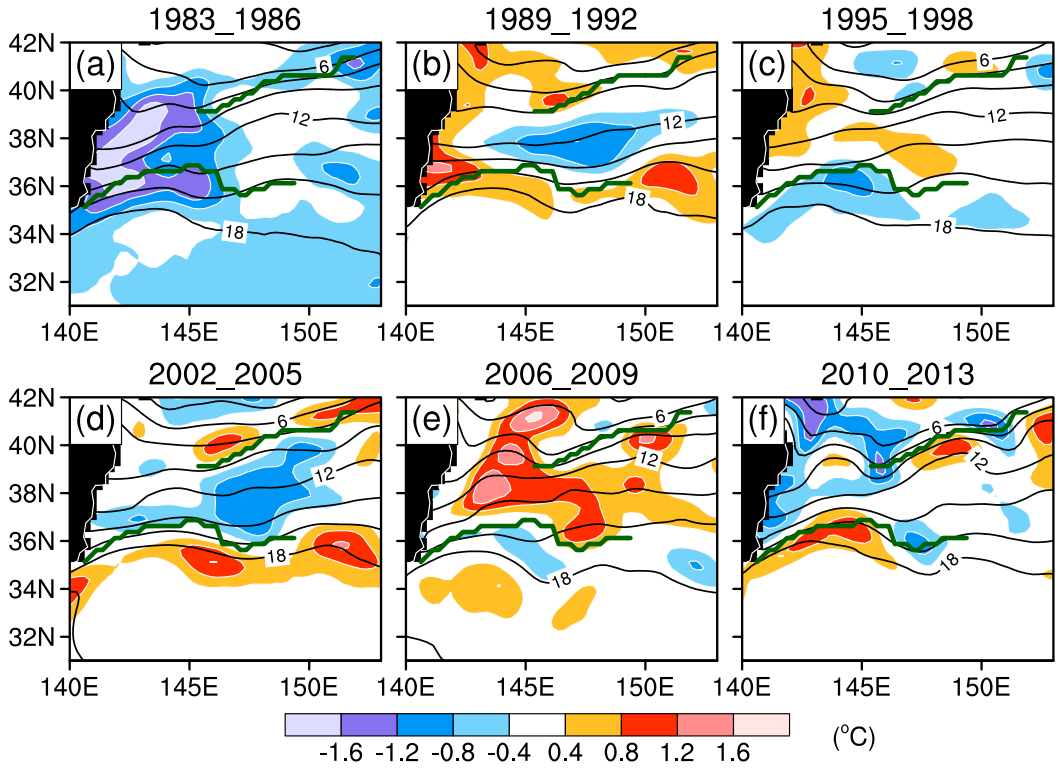

FIG. 3. Wintertime (December–March) SST (contoured every 2°C) and its anomalies from wintertime climatology for 1982–2014 (shaded), both averaged in the 4-yr periods indicated. Green lines indicate the KE and Oyashio fronts at which the climatological-mean equatorward SST gradient maximizes locally.

mid-1980s (Fig. 3a), the southward Oyashio along the east coast of Japan was very strong with the southward-displaced SAFZ, leading to overall cooling over the KOE region with the extreme cooling along the Japanese east coast (Nakamura and Kazmin 2003; Nonaka et al. 2006). Since the late 1980s, the pattern of the dominant decadal SST variability over the North Pacific has changed (Miyasaka et al. 2014). Indeed, anomalies observed in the later periods are characterized by a dipolar anomaly pattern even in the unfiltered SST fields (Figs. 3b–f). For these reasons, we limit our attention to the period since 1989 in the following analysis.

Composites of wintertime SST and its meridional gradient based on the OISST data are constructed separately for the unstable (Fig. 4a) and stable (Fig. 4b) KE regimes defined with KEI for the 1989–2014 period. The composite analysis excludes near-normal winters, for which the absolute values of winter-mean KEI are less than 25% of its standard deviation for 1989–2014 (i.e., 1989, 1994, and 2001; open circles in Fig. 1a). As a consequence, 13 (10) winters are chosen for the stable (unstable) regime within 1989–2014. In all of the following analyses, statistical significance of composited differences is estimated through Student's t test in assuming that anomalies in individual winters are mutually independent. The KE front along 36°N is particularly distinct in the stable regime, while it is substantially weaker in the unstable regime (Figs. 4a,b). The composited difference in SST (Fig. 4c) indicates zonally elongated dipolar anomalies in good correspondence to the leading EOF pattern of hSST (Fig. 2a). In the unstable KE regime, more warm-core eddies are detached from the KE jet northward (Sugimoto and Hanawa 2011; Seo et al. 2014; Sasaki and Minobe 2015). Therefore, SST is higher than normal to the north of the mean KE jet, and the Oyashio front located to the north tends to be stronger in showing its southwest–northeast orientation more distinctly. The variability of the Oyashio front may be viewed as modulation of a northeastward quasi-stationary jet (Isoguchi et al. 2006; Wagawa et al. 2014).

Note that previous studies have shown that warm SST anomalies are formed in the stable KE regime to the east of 155°E with time lags of one or two months after KEI peaks (Qiu et al. 2014; Révelard et al. 2016). Since modulations of the eastward transport make the dominant contribution to the formation of SST anomalies in the eastern region (Sugimoto 2014) rather than

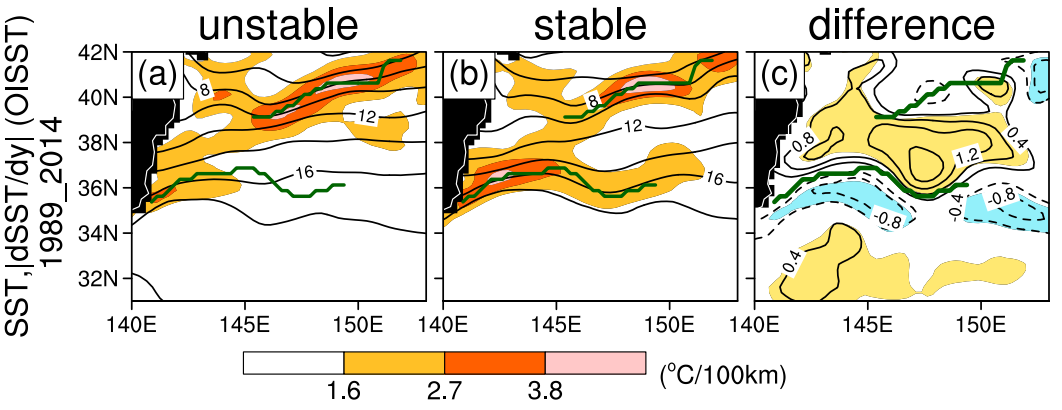

FIG. 4. Wintertime (December–March) SST (contoured every 2°C) and its equatorward gradient [°C (100 km)$^{-1}$; shaded as indicated at the bottom] composited for the (a) unstable and (b) stable regimes of KE on the basis of the KEI (black line in Fig. 1a). (c) Composite difference (unstable − stable) of SST (contoured every 0.4°C; dashed for negative; zero contours are omitted). Shading is applied where the SST difference is statistically significant at the 90% confidence level. Green lines indicate the axes of the KE and Oyashio fronts at which climatological-mean equatorward SST gradient maximizes locally.

oceanic eddies, the sign of SST anomalies tends to be reversed. In fact, the present composite analysis shows a weaker but significant negative (positive) SST anomaly to the east of 155°E in the unstable (stable) KE regime (not shown), which is consistent with the previous studies. Seasonality should also be taken into consideration when compared with the previous studies.

In Fig. 2a, a zonal belt of negative SST anomalies at 35°N is a manifestation of the weakened KE jet. These results indicate that KEI well captures the decadal-scale KE variability and associated mesoscale SST variability since the late 1980s. In the next subsection, we investigate the imprints of the SST anomalies on mesoscale atmospheric fields.

b. *Composite analysis of satellite-based observational data*

Figure 5 shows wintertime climatologies of several variables and standard deviation of their interannual variability over the KOE region based mainly on satellite data. Coinciding with the maximum SST variability along the KE front (Fig. 5a), interannual variability maximizes also in turbulent heat fluxes (Fig. 5b) and total cloud amount (TCA) (Fig. 5c). Although less organized, interannual variability of surface wind convergence (Fig. 5d) is also locally augmented near the KE front. By contrast, augmentation of precipitation variability is less obvious along the KE front (Fig. 5e), but the augmentation is still noticeable east of 145°E.

Wintertime composites indicate stronger meridional confinement of large upward turbulent heat fluxes into the KE jet in its stable regime (Fig. 6b) than in the unstable regime (Fig. 6a). The difference between the two regimes is characterized by anomalous heat fluxes within the mixed water region (Fig. 6c), which are significantly positive in the unstable regime in correspondence to higher SST (Fig. 4c). Indeed, the SST anomalies make the dominant contribution to the heat flux anomalies, as discussed in section 5. When the meridional high-pass filtering is applied to the heat fluxes [h(SHF+LHF)], their negative anomalies along 35°N also become statistically significant (blue hatched areas in Fig. 6c) over the negative SST anomalies along the climatological KE axis (Fig. 4c). Qualitatively the same results can be obtained for turbulent heat fluxes if based on the Japanese Ocean Flux Datasets with Use of Remote Sensing Observations version 2 (J-OFURO2) (Kubota and Tomita 2007).

Composites for TCA exhibit characteristics that are similar to those for the heat fluxes; that is, TCA is particularly high around the KE in its stable regime (Fig. 6e), while TCA is higher broadly over the KOE region in the unstable regime (Fig. 6d). The difference composite map in Fig. 6f thus features a meridional dipolar pattern of TCA anomalies with positive anomalies in the mixed water region, coinciding with enhanced upward heat fluxes (Fig. 6c) and surface wind convergence (Fig. 6i). Although those differences in the unfiltered TCA composites are not highly significant, the corresponding difference in the meridionally high-pass-filtered TCA (hTCA) field exhibits higher statistical significance (red and blue hatched areas in Fig. 6f). In fact, confidence intervals of zonally averaged hTCA in the stable KE regime show that the upper confidence limits at its local minimum (i.e., 36.5°N) (red horizontal lines in Fig. 7b) is smaller than lower limits at local maxima near the KE and Oyashio fronts (i.e., 34.5° and

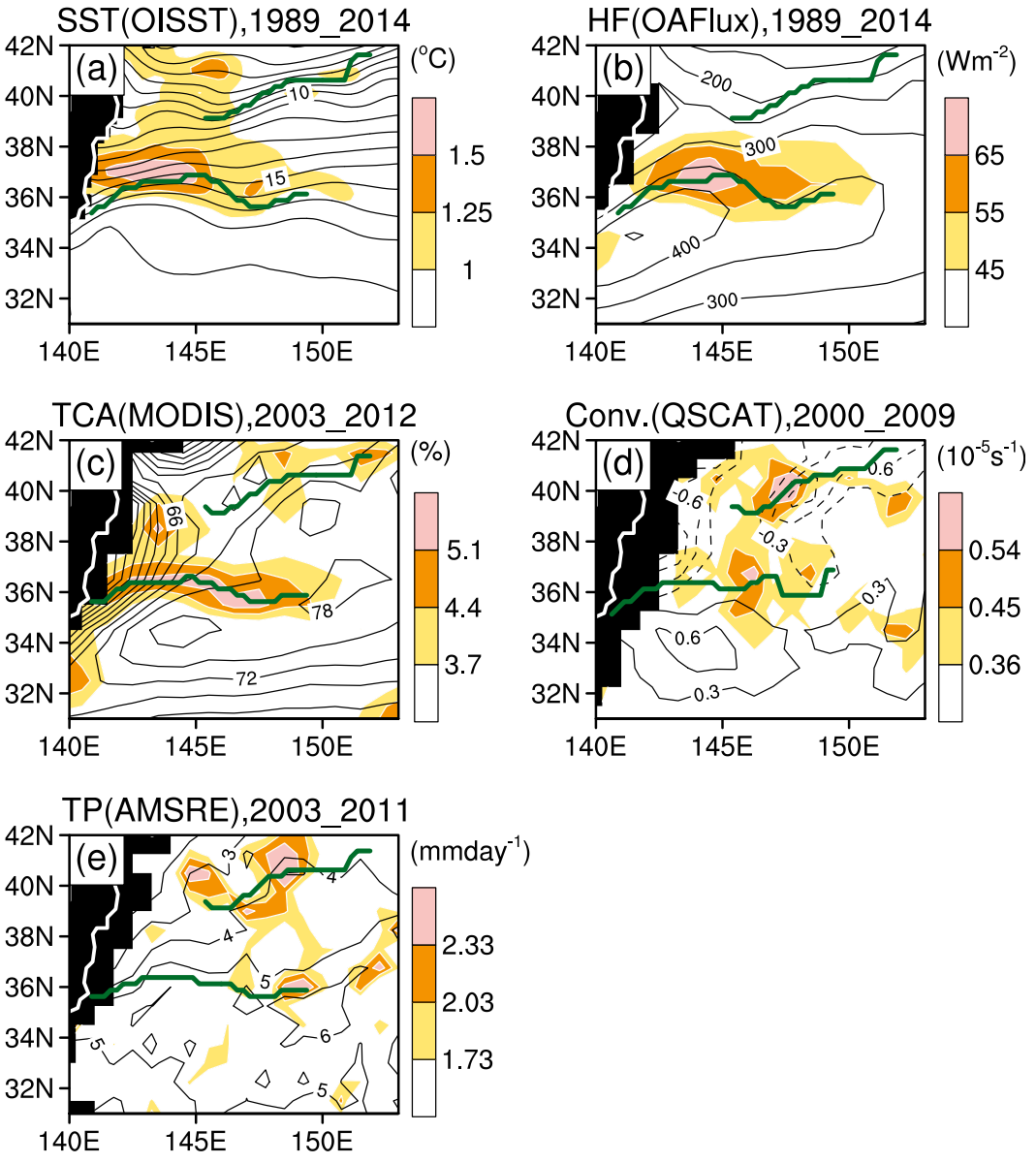

FIG. 5. Wintertime (December–March) climatologies (contoured) and std dev of interannual variability (shaded as indicated at the right of each panel) of (a) SST (OISST; contoured every 1°C), (b) surface sensible and latent heat fluxes combined (OAFlux; contoured every 50 W m^{-2}; upward positive), (c) MODIS TCA (contoured every 3%), (d) QuikSCAT surface wind convergence interpolated onto 0.75° grid intervals (contoured every 0.3 × 10^{-5} s^{-1}; dashed for divergence; zero contours are omitted), and (e) AMSR-E total precipitation interpolated onto 0.75° grid intervals (contoured every 1 mm day^{-1}) for the periods indicated. Green lines indicate the KE and Oyashio fronts at which climatological-mean equatorward SST gradient maximizes locally.

39.5°N), while no peaks are identified in the unstable KE regime (Fig. 7a). This result suggests that the dual-peak profile on hTCA may be robust only in the stable KE regime. Furthermore, the heterogeneous regression pattern of hTCA (Fig. 2b) with its leading SVD time series with hSST (red line in Fig. 1a) shows a distinct meridional dipolar pattern of anomalous hTCA. The leading SVD mode between hTCA and hSST explains as much as 53% of their squared covariance, and the correlation between their SVD time series reaches as high as +0.96, indicative of their strong covariability. Although the statistical significance is not necessarily high in the composited difference in AMSR-E precipitation (Fig. 6l), a well-defined precipitation band forms along the warm KE jet in its stable regime (Fig. 6k), while it becomes less evident in the unstable regime (Fig. 6j). In

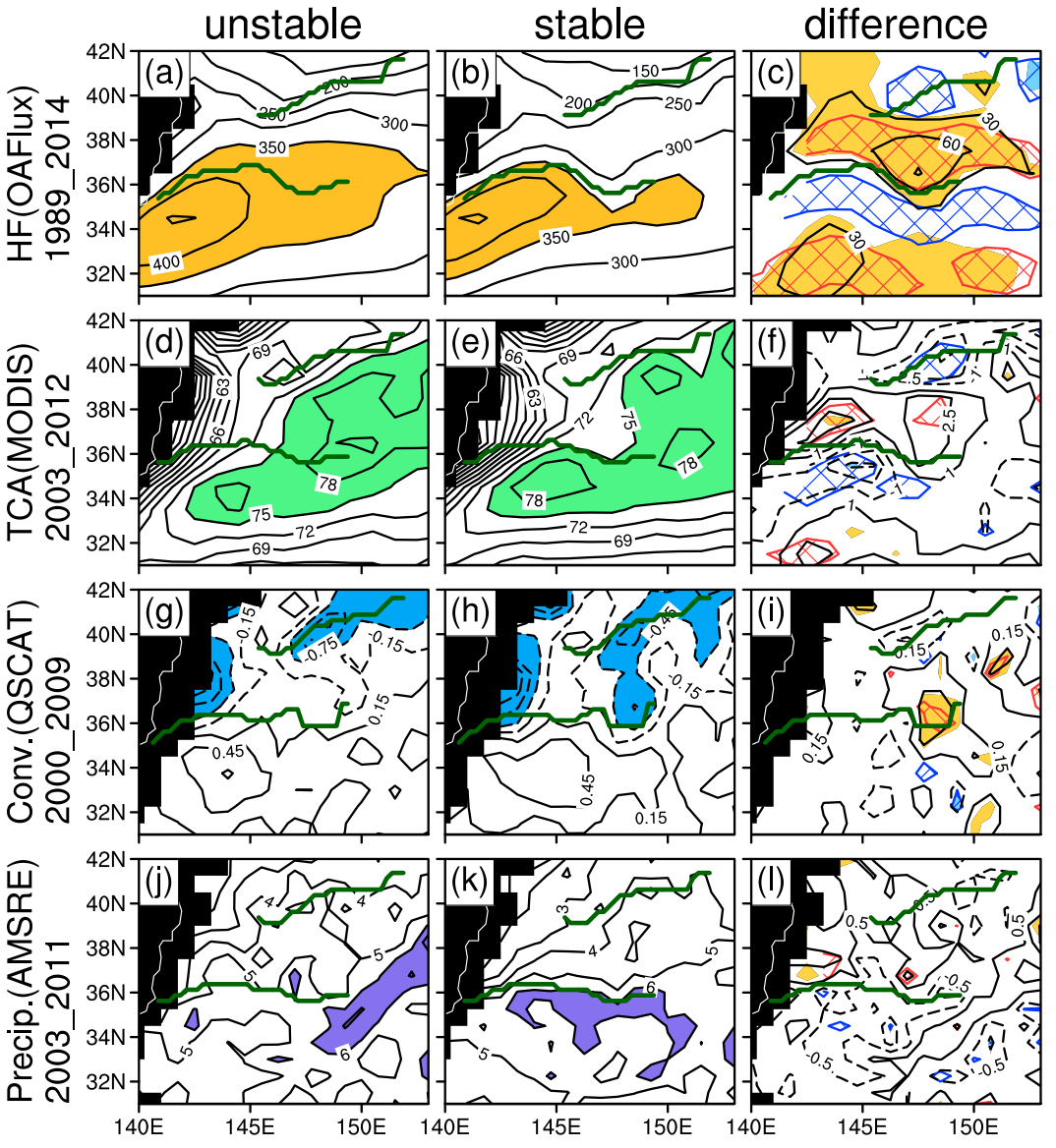

FIG. 6. (a),(b) As in Figs. 4a,b, but for turbulent heat fluxes (SHF + LHF) (contoured every 50 W m^{-2}; shaded in yellow where its values exceed 350 W m^{-2}) based on the OAFlux data (1989–2014) and (c) the difference (contoured every 30 W m^{-2}; zero contours are omitted). (d),(e) As in (a),(b), but for MODIS TCA (2003–12) (contoured every 3%; shaded in green where the values exceed 75%) and (f) the difference (contoured at intervals of 1.5% starting from ±1%). (g),(h) As in (a),(b), but for QuikSCAT surface wind convergence (2000–09) (contoured at intervals of 0.3×10^{-5} s^{-1} starting from $\pm 0.15 \times 10^{-5}$ s^{-1}; dashed for divergence; shaded in blue where the values are below -0.45×10^{-5} s^{-1}) and (i) the difference (contoured at intervals of 0.3×10^{-5} s^{-1} starting from $\pm 0.15 \times 10^{-5}$ s^{-1}). (j),(k) As in (a),(b), but for AMSR-E precipitation (2003–11) (contoured every 1 mm day^{-1}; shaded in purple where the values exceed 6 mm day^{-1}) and (l) the difference (contoured at intervals of 1 mm day^{-1} starting from ±0.5 mm day^{-1}). For (c),(f),(i),(l), shading is applied locally where the difference is statistically significant at the 90% confidence level, and red and blue hatched areas are overlaid where the corresponding positive and negative differences, respectively, in their meridionally high-pass-filtered values are statistically significant at the same level.

fact, enhancement in meridionally high-pass-filtered precipitation (hPrecip) along the KE axis (35.25°N) relative to the mixed water region (38.25°N) is identified as a robust feature only in the stable KE regime (Fig. 7d). These results are indicative of local influence of SST variability associated with changing dynamical regimes of the KE on mesoscale atmospheric fields through modulated hydrostatic effect and/or vertical mixing effect.

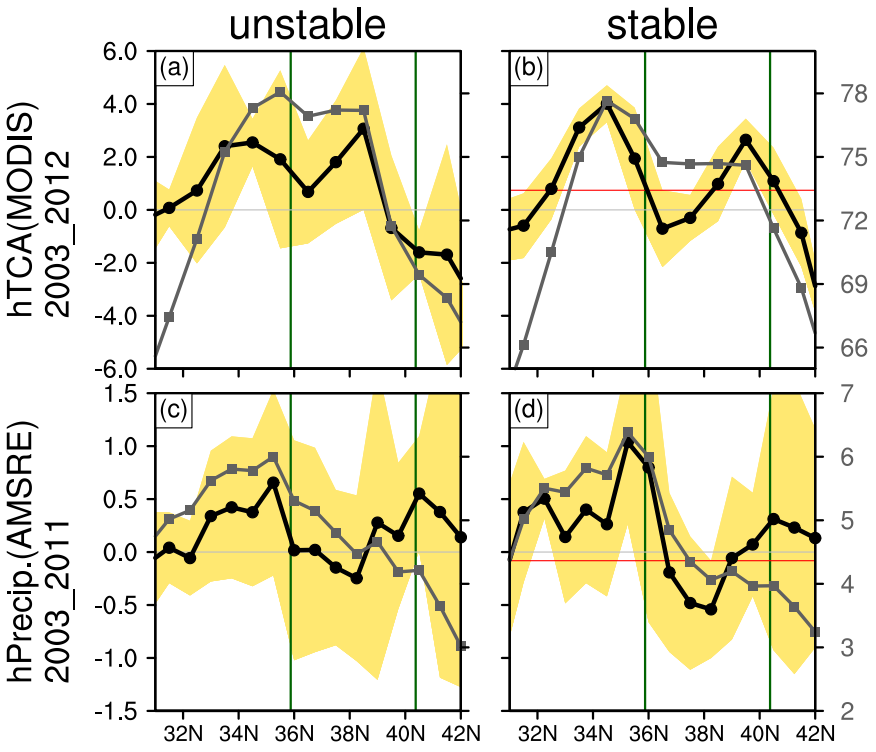

FIG. 7. (a),(b) Meridional profiles of MODIS TCA (%; gray lines, right y axis) and its meridionally high-pass-filtered profiles (%; black lines, left y axis) from Figs. 6d and 6e, respectively, after they are averaged zonally over 146.5°–149.5°E. Vertical green lines indicate the KE and Oyashio fronts at which equatorward SST gradient maximizes climatologically. Yellow shading represents the 90% confidence intervals of the zonally averaged high-pass-filtered fields (i.e., black lines), estimated from the t distribution with $N - 1$ degrees of freedom, where N denotes the number of years for each composite. (c),(d) Same as in (a),(b), but for AMSR-E precipitation (mm day^{-1}) from Figs. 6j and 6k, respectively, averaged zonally over 146.25°–150°E. Red horizontal lines indicate the upper bounds of the confidence intervals at 36.5°N in (b) and 38.25°N in (d).

4. Interannual variability of mesoscale atmospheric fields based on the ERA-Interim data

a. Interannual variability in the high-resolution SST period

Masunaga et al. (2015) have found that wintertime climatologies based on the ERA-Interim data for the period from 2002 to 2012, in which horizontal resolution of prescribed SST has been improved, represent mesoscale atmospheric structures in a manner consistent with satellite observations. In this section, we investigate interannual variability of mesoscale atmospheric fields represented in the ERA-Interim under the influence of the KE variability. Unlike for other winters, the winter mean for 2002 is defined as the January–March (JFM) mean because December 2001 is included in the LR period.

Figure 1b shows the leading PC time series of hSST prescribed for the ERA-Interim. Note that the time series are constructed separately for the periods 1979–2001 and 2002–14. Since 2002, the leading EOF captures mesoscale SST variability associated with the regime changes of KE. In fact, we have confirmed that anomaly composites of SST, turbulent heat fluxes, and their meridionally high-pass-filtered fields in the ERA-Interim are similar to those in OISST (Fig. 4) and OAFlux (Figs. 6a–c), respectively (not shown).

The ERA-Interim constructed with the high-resolution SST overall reproduces mesoscale atmospheric variability under the influence of the KE regime changes (Fig. 8), as captured by satellite observations (Fig. 5). Interannual standard deviations of SST and turbulent heat fluxes are locally enhanced along 36°N to the north of the KE jet (not shown), in association with locally enhanced standard deviation of hSLP (Fig. 8c) and surface wind convergence (Fig. 8a). Nevertheless, variability in surface wind convergence is particularly enhanced in the ERA-Interim within a southwest–northeast-oriented

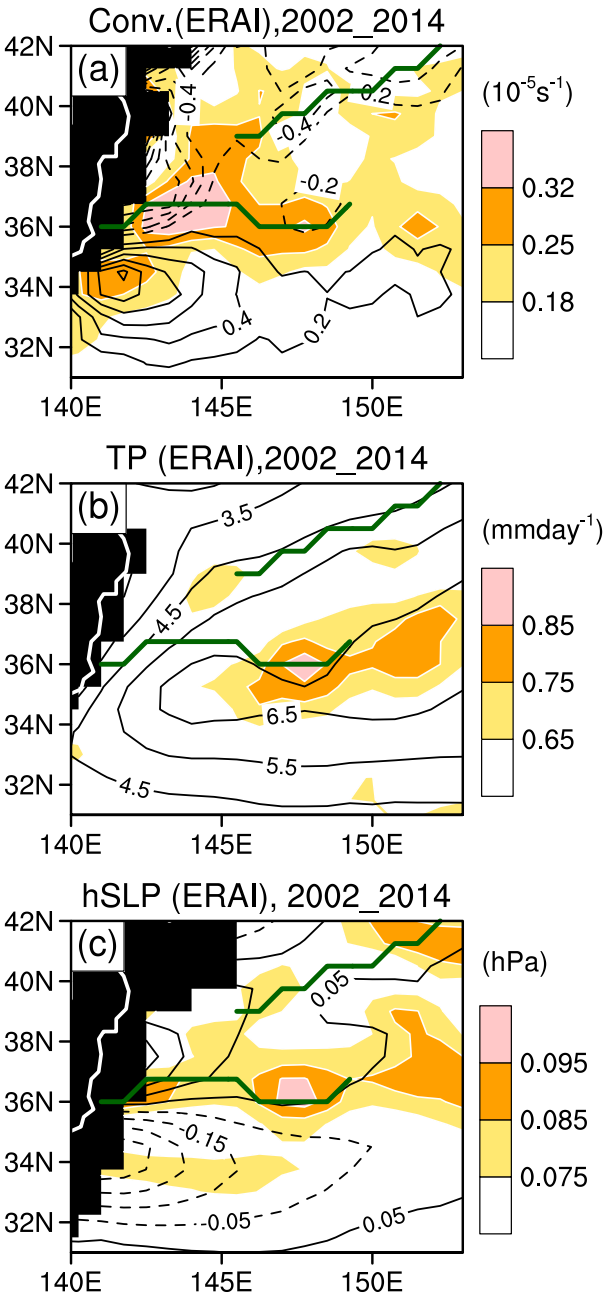

FIG. 8. As in Fig. 5, but only fields based on the ERA-Interim for the HR period (2002–14). (a) Surface wind convergence (contoured every $0.2 \times 10^{-5}\,s^{-1}$; dashed for divergence; zero contours are omitted), (b) total precipitation (contoured every 1 mm day^{-1}), and (c) hSLP (contoured at intervals of 0.1 hPa from ±0.05 hPa; dashed for negative).

region just off the east coast of Japan (Fig. 8a), but the corresponding signature is much weaker in the QuikSCAT data (Fig. 5d). Meanwhile, the wintertime climatology in surface wind convergence and divergence in the ERA-Interim is overall weaker than those in QuikSCAT, if compared only for the overlapped period [i.e., 2002–09 (not shown)]. These differences can be attributed to the poor representation of MABL process in the forecast model, as discussed in Song et al. (2009). In spite of these differences, the composited anomalies in wind convergence in the ERA-Interim (Fig. 9c) can overall reproduce those observed in QuikSCAT data (Fig. 6i). Wintertime composites of TCA for the stable (Fig. 9e) and unstable (Fig. 9d) KE regimes are similar to the respective composites based on the MODIS data (Figs. 6e and 6d, respectively), while the enhancement of TCA over the mixed water region in the unstable regime is statistically significant even in the unfiltered field (Fig. 9f). This enhanced cloudiness is consistent with a significant positive anomaly in surface wind convergence (Fig. 9c) and a cyclonic hSLP anomaly (Fig. 10c) in the mixed water region.

Interannual variability of total precipitation in the ERA-Interim is also locally augmented in the mixed water region to the north of the mean KE jet (Fig. 8b). Although the anomalies in unfiltered total precipitation in the mixed water region are not highly significant (Fig. 9i), the corresponding enhancement in convective precipitation is more significant (Fig. 10f) and consistent with significant cyclonic hSLP anomaly, significant enhancement of surface wind convergence (Fig. 9c), TCA (Fig. 9f), and surface heat fluxes (not shown). Since large-scale precipitation (Figs. 10g–i) is not as sensitive to SST as convective precipitation, it may act to obscure the imprints of SST variability on total precipitation in both the satellite data (Figs. 6j–l) and reanalysis (Figs. 9g–i).

b. *Meridional–vertical structure of mesoscale features within MABL*

In this subsection, we investigate imprints of the KE variability on the vertical structure of MABL represented in the ERA-Interim. Figure 11 shows meridional sections of wintertime composites for the unstable (Figs. 11a–d) and stable (Figs. 11e–h) KE regimes in addition to their differences (Figs. 11i–l), constructed for 147.75°E, the meridian along which the strongest negative hSLP anomaly is observed (Fig. 10c). In the stable KE regime, meridionally high-pass-filtered virtual potential temperature ($h\theta_v$) within the MABL exhibits a dual-peak profile (represented with shading in Fig. 11f and a red line in Fig. 11e) associated with distinct dual peaks in both hSST and h(SHF+LHF) (blue and red lines in Fig. 11g, respectively), one to the south of the mean KE jet and the other around the Oyashio front. Furthermore, these peaks coincide with local hSLP minima and local maxima in ascent (black contours in Fig. 11f and black line in Fig. 11e), surface wind convergence (red line in Fig. 11h), and MABL height (gray

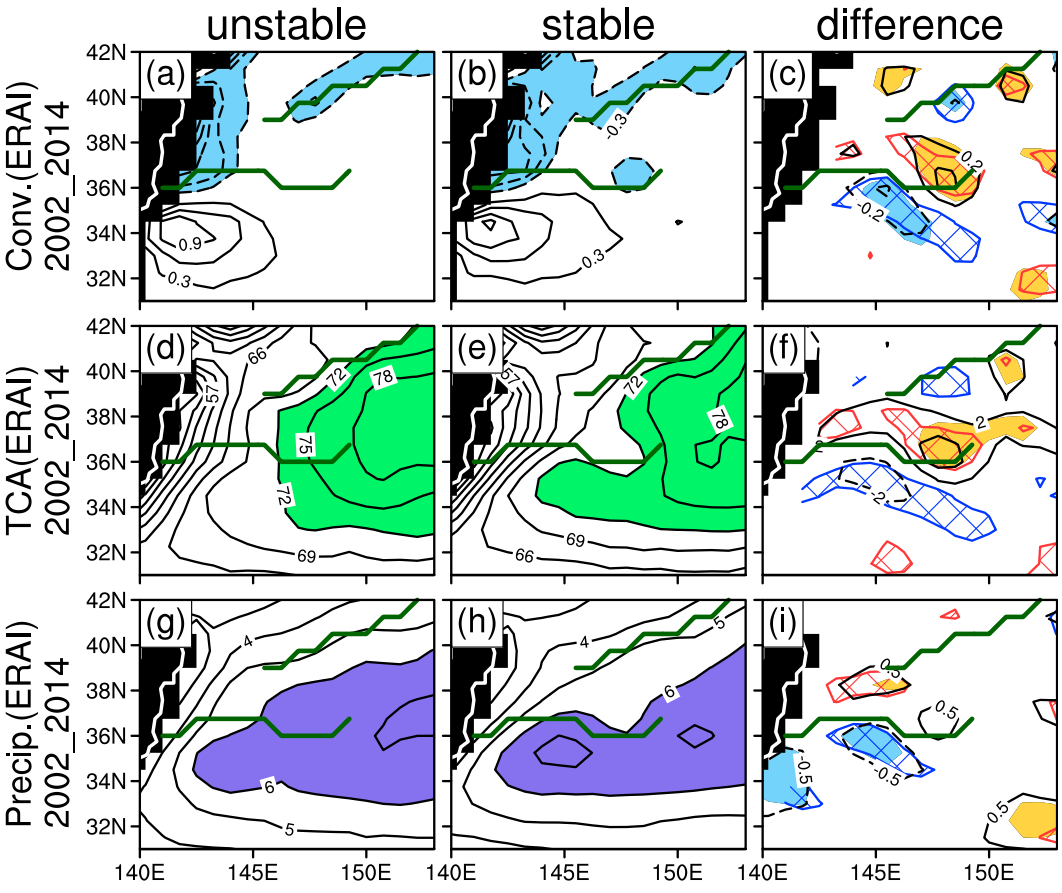

FIG. 9. As in Fig. 6d–l, but based on the ERA-Interim for the HR period (2002–14). (a),(b) Surface wind convergence (contoured every $0.3 \times 10^{-5}\,s^{-1}$; dashed for divergence; zero contours are omitted; shaded in blue where its values are below $-0.3 \times 10^{-5}\,s^{-1}$) and (c) the difference (contoured every $0.2 \times 10^{-5}\,s^{-1}$; dashed for negative; zero contours are omitted). (d),(e) TCA (contoured every 3%; shaded in green where its values exceed 72%) and (f) the difference (contoured every 2%; dashed for negative; zero contours are omitted). (g),(h) Total precipitation (contoured every 1 mm day^{-1}; shaded in purple where its values exceed 6 mm day^{-1}) and (i) the difference (contoured every ± 0.5 mm day^{-1}; dashed for negative; zero contours are omitted).

line in Fig. 11f). In contrast, such dual-peak profiles as above are almost absent in the unstable KE regime; a local extreme of each of the variables near the mean KE front is much weaker and meridionally broader (Figs. 11a–d) if compared with its counterpart in the stable regime. The composited differences show statistically significant anomalies in the mixed water region (marked with circles in Figs. 11i–l). We have confirmed that the composited distributions of meridionally high-pass-filtered virtual air temperature and their difference within the MABL can well explain the composited hSLP anomalies' thorough hydrostatic relationship (not shown). These results are indicative of the hydrostatic effect modulated under the KE regime changes. Indeed, high-pass-filtered wind vectors composited separately for the two KE regimes and their differences tend to be divergent over positive hSLP and convergent over negative hSLP (Figs. 12a–c). In fact, the interannual correlation (-0.86) is significant between winter-mean anomalies in hSLP and surface wind convergence if averaged over the mixed water region 35.25°–37.5°N, 147°–149.25°E. Although most of the significant anomalies are confined into MABL, significant anomalies in vertical motion are found to reach the 750-hPa level (not shown) as imprints of the KE variability in the free troposphere.

c. *Zonal–vertical structure of mesoscale features within MABL*

Although the results above suggest the importance of the hydrostatic effect, the vertical mixing effect can also play an important role. In fact, Tanimoto et al. (2011) argued that a combination of these two effects climatologically yields a characteristic distribution of near-surface ageostrophic winds around the SLP trough along the KE. Actually, composited differences in surface zonal wind speed show significant enhancement (red

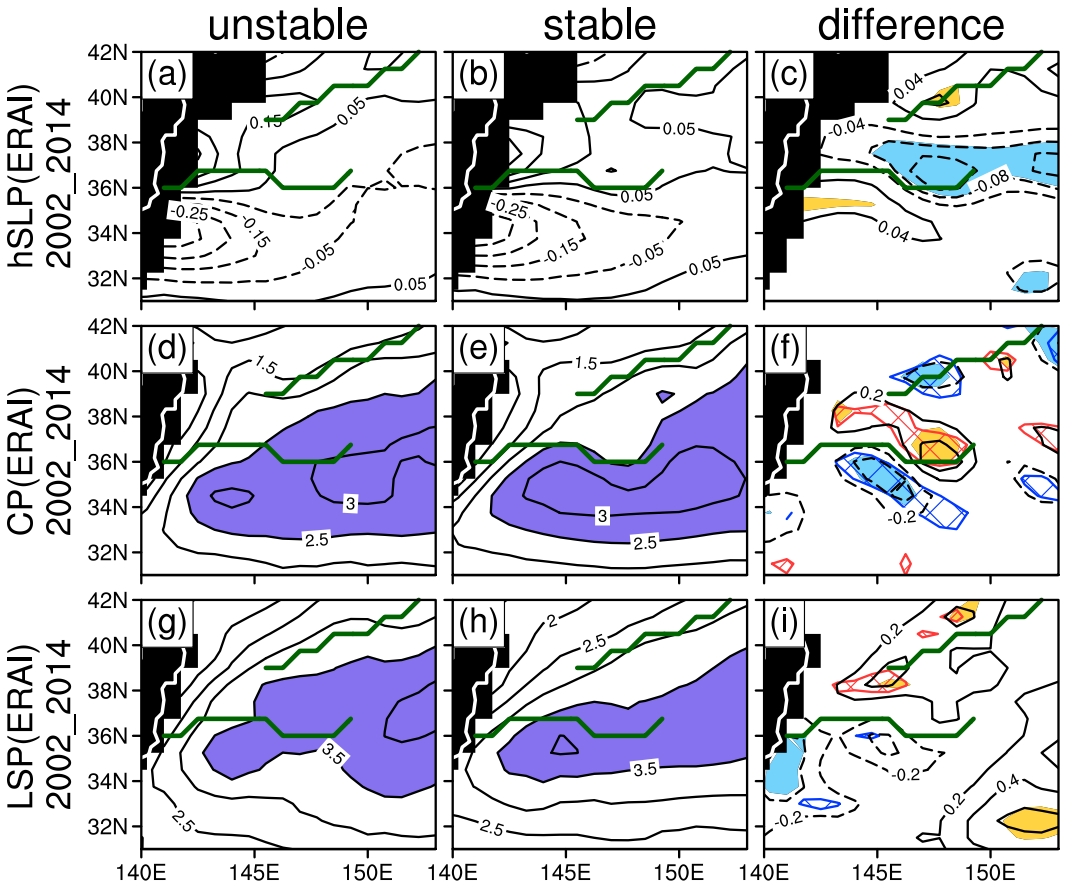

FIG. 10. As in Fig. 9, but for (a),(b) hSLP (contoured at intervals of 0.1 hPa starting from ±0.05 hPa) and (c) the difference (contoured every 0.04 hPa); (d),(e) convective precipitation (contoured every 0.5 mm day^{-1}; shaded in purple where its values exceed 2.5 mm day^{-1}) and (f) the difference (contoured every 0.2 mm day^{-1}); and (g),(h) large-scale precipitation (contoured every 0.5 mm day^{-1}; shaded in purple where its values exceed 3.5 mm day^{-1}) and (i) the difference (contoured every 0.2 mm day^{-1}). Zero contours are omitted.

arrows in Fig. 12d) near the warm SST anomaly in the mixed water region (shaded in Fig. 12d), which can be a manifestation of enhanced downward transport of westerly momentum as the vertical mixing effect. In fact, the westerlies are prevailing above the 850-hPa level (not shown).

To gain further insights into the mesoscale atmospheric structures in the KOE region, zonal sections are constructed for 36.75°N (Figs. 13j–r), the latitude at which composited SST anomalies are strongest in the mixed water region. In the stable KE regime, zonal variations are distinct in unfiltered SST (blue line in Fig. 13o) and its zonal gradient (dSST/dx) (purple line in Fig. 13n) in the presence of weak but persistent meanders of the intensified KE associated with anticyclonic eddies located at 144° and 150°E (e.g., Qiu and Chen 2005). Local maxima (minima) of the converging zonal component of surface winds (i.e., $-du_s/dx$ at the lowest model level) (red line in Fig. 13n) roughly correspond to local minima (maxima) of zonally high-pass-filtered SLP (zhSLP) (black lines in Fig. 13o) with slight phase shift. These zonal variations are, by contrast, much weaker in the unstable KE regime (Figs. 13k–l), reflecting the weaker KE. The composited difference in $-du_s/dx$ (Fig. 13q) and zhSLP (Fig. 13r) exhibits significant anomalies that correspond to each other. Again, we have confirmed that these zhSLP fields are well reproduced from zonally high-pass-filtered virtual temperature within MABL through hydrostatic relation (not shown), suggestive of the modulated hydrostatic effect due to the KE variability. Nevertheless, dSST/dx exhibits a nearly out-of-phase relationship with $-du_s/dx$ only in the stable KE regime (purple and red lines in Fig. 13n), which is well reflected in their composited differences (Fig. 13q). This is indicative of the vertical mixing effect (e.g., Hayes et al. 1989), the zonal variations of which are stronger in the stable KE regime. Over the warmer (cooler) SST, the stronger (weaker)

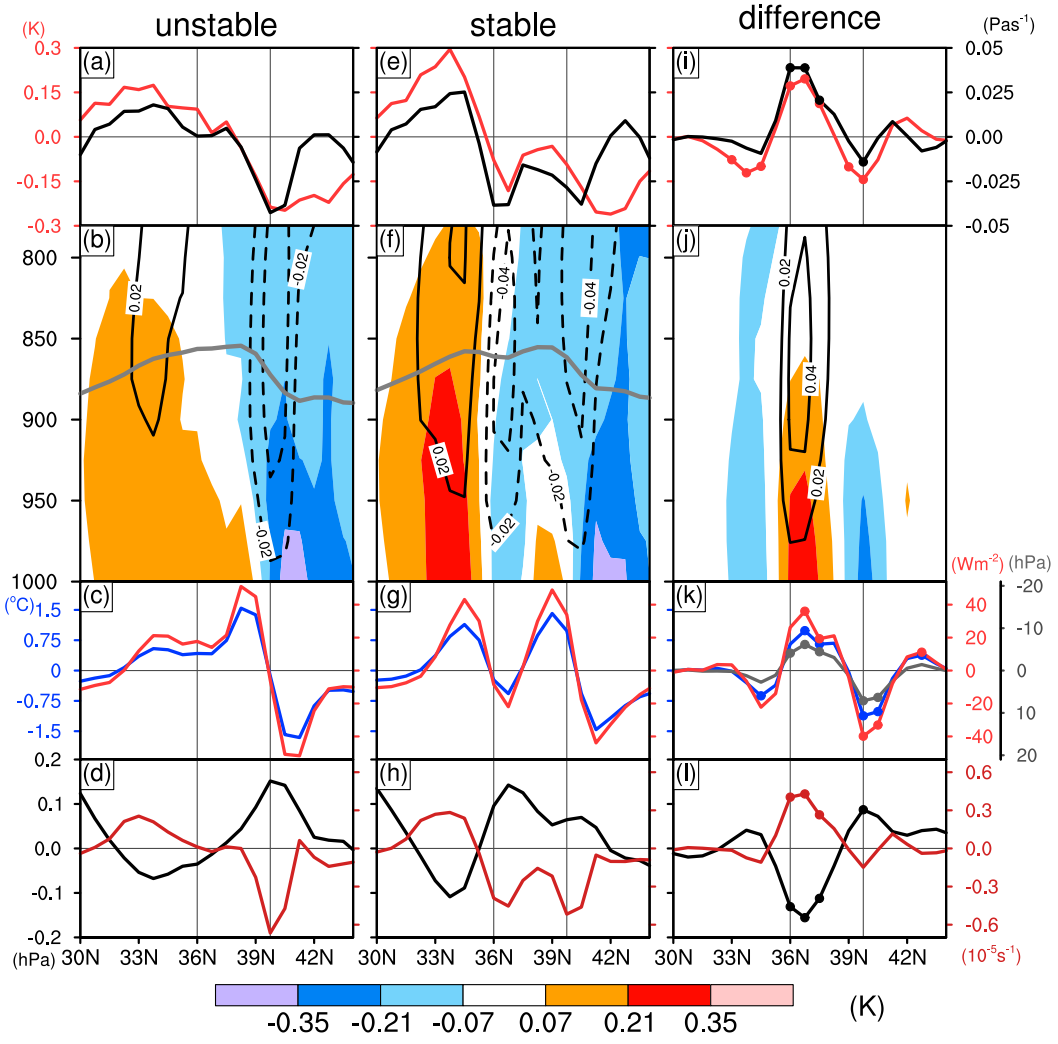

FIG. 11. (a) Latitudinal profiles of $-\omega$ (black line, right y axis) and $h\theta_v$ (red line, left y axis) at 925 hPa for the unstable KE regime. (b) Winter-mean meridional cross section of $-\omega$ along 147.75°E (contoured every 0.02 Pa s^{-1}; dashed for descending velocity; zero contours are omitted), $h\theta_v$ (K; shaded as indicated at the bottom of the figure), and MABL top (gray line), composited for the unstable KE regime on the basis of the ERA-Interim (2002–14). (c) As in (a), but for hSST (blue line, left y axis) and h(SHF+LHF) (red line, right red y axis) (d) As in (a), but for hSLP (black line, left y axis) and surface wind convergence (dark red line, right y axis). (e)–(h) As in (a)–(d), but for the stable KE regime. (i)–(l) As in (a)–(d), but for the corresponding differences. Gray line in (k) indicates the composited difference in meridionally high-pass-filtered pressure at top of boundary layer (hPa; right gray y axis). In (i),(k),(l), the composited differences that are significant at the 90% confidence level are marked with small circles. Vertical thin lines in (a),(c)–(e),(g)–(i),(k),(l) indicate the KE and Oyashio fronts at which the climatological-mean meridional SST gradient maximizes locally.

vertical mixing effect acts to enhance (weaken) the westerly component at the surface, leading to the enhanced $-du_s/dx$. In the unstable regime, by contrast, zonal variations in the vertical mixing effect are virtually missing under the weakened zonal SST gradient (Figs. 13k–l). Rather, vertical shear in lower-tropospheric zonal wind (du/dz) is overall weaker significantly in the unstable KE regime (shading and yellow hatched areas in Fig. 13p), especially over the significant positive SST anomaly (blue line in Fig. 13r).

Similar features to those discussed above are found also in zonal sections for 40.5°E (Figs. 13a–i), the latitude at which dSST/dx is enhanced near the Oyashio front. Although the KE varied almost independently of the Oyashio (e.g., Nonaka et al. 2006), the Oyashio front during our analysis period tended to be stronger in the unstable KE regime because of warm SST in the mixed water region (Fig. 4). Owing to its southwest–northeast orientation, the Oyashio front is characterized by strong dSST/dx, which is enhanced in the unstable KE regime

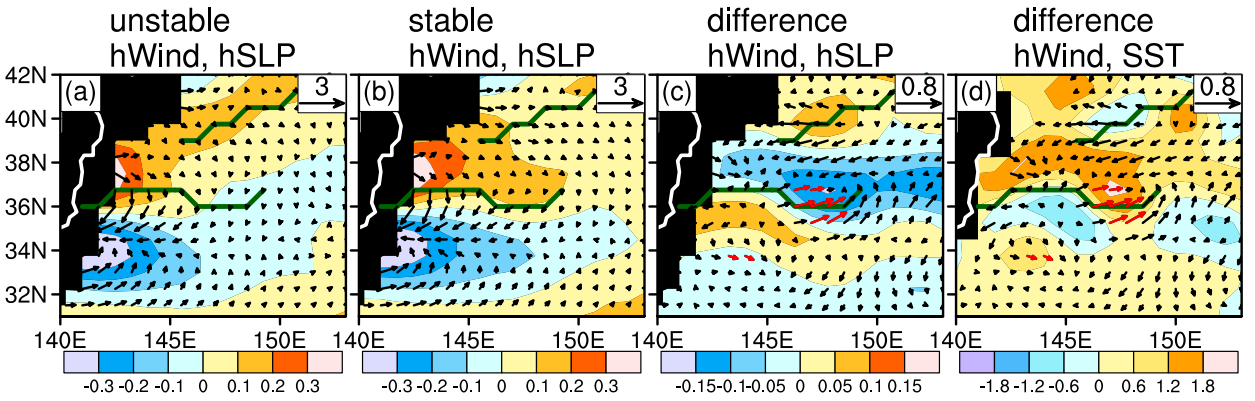

FIG. 12. (a),(b) As in Fig. 10(a),(b), but for meridionally high-pass-filtered wind vectors at the lowest model level ($m\,s^{-1}$; arrows as indicated on the top right of the panels) and hSLP (hPa; shaded as indicated below the panels) and (c) the difference (unstable − stable). (d) As in (c), but for SST (°C) in place of hSLP. Red arrows are applied in (c),(d) where the composited differences of meridionally high-pass-filtered zonal wind are statistically significant at the 90% confidence level.

(Fig. 13b) in the presence of the warm SST anomaly within the mixed water region (Fig. 4). Because of the vertical mixing effect, converging surface zonal wind is stronger in the unstable KE regime (Figs. 13b,c) than in the stable regime (Figs. 13e,f), as opposed to the situation near the KE front. We therefore conclude that both the hydrostatic and vertical mixing effects can be operative in winter over the KOE region. They are found to undergo substantial modulations under the changing dynamical regimes of the KE, giving rise to decadal-scale modulations in the surface wind field.

For more quantitative investigation, however, which is beyond the scope of the present study, horizontal wind shear in the free troposphere should be taken into consideration, which can modulate surface wind convergence and divergence fields. Moreover, unlike our simple winter-mean fields, we should have constructed composites based on daily fields selected separately for different background wind speeds and directions relative to the local SST gradient, to which surface wind convergence and divergence can be particularly sensitive (e.g., Kilpatrick et al. 2014; Schneider and Qiu 2015).

d. Interannual variability in the low-resolution SST period of the ERA-Interim

In this subsection, the same composite analysis as above is applied to the ERA-Interim, but for the 13-yr period from 1989 to 2001, in which horizontal resolution of the prescribed SST data is insufficient to represent the separation between the KE and Oyashio fronts. According to the KEI, the KE was stable in four winters and unstable in six winters during this period (as indicated with closed circles in Fig. 1a). Applied to SST and turbulent surface heat fluxes in winter based on the OISST and OAFlux data, respectively, our composite analysis for this period reveals meridionally confined significant anomalies (not shown) similar to those obtained for the more recent years (Figs. 4 and 6a–c, respectively), although the significant anomalies in the turbulent heat fluxes are somewhat broader meridionally. However, the corresponding composites based on the ERA-Interim in Fig. 14 seem substantially different; unfiltered SST anomalies used for the ERA-Interim are not significant in the composite difference map (Fig. 14c). Although some of the corresponding anomalies in the meridionally high-pass-filtered SST are statistically significant, they are meridionally broadened and less than half in strength if compared to the corresponding OISST anomalies. Likewise, the composites and their difference of turbulent heat fluxes based on the ERA-Interim (Figs. 14d–f) represent meridionally broader features than those based on the OAFlux. The corresponding differences in surface wind convergence (Fig. 14i), TCA (Fig. 14l), and hSLP (not shown) exhibit no significant anomalies at 37°N, unlike in the ERA-Interim HR period. These results elucidate the importance of high-resolution SST prescribed for atmospheric data assimilation.

5. Assessing the dominant factors in determining heat fluxes anomalies

Sugimoto and Hanawa (2011) suggested that SST anomalies are of primary importance in determining turbulent heat flux anomalies associated with the KE regime change. To identify the dominant factors in determining anomalous heat fluxes in our composites (Figs. 6a–c), we utilize the linearized bulk aerodynamic formulas used by Tanimoto et al. (2003). The bulk aerodynamic formulas for SHF and LHF may be written as

$$\mathrm{SHF} = \rho_a C_p C_H W_a (T_s - T_a) \qquad (1)$$

and

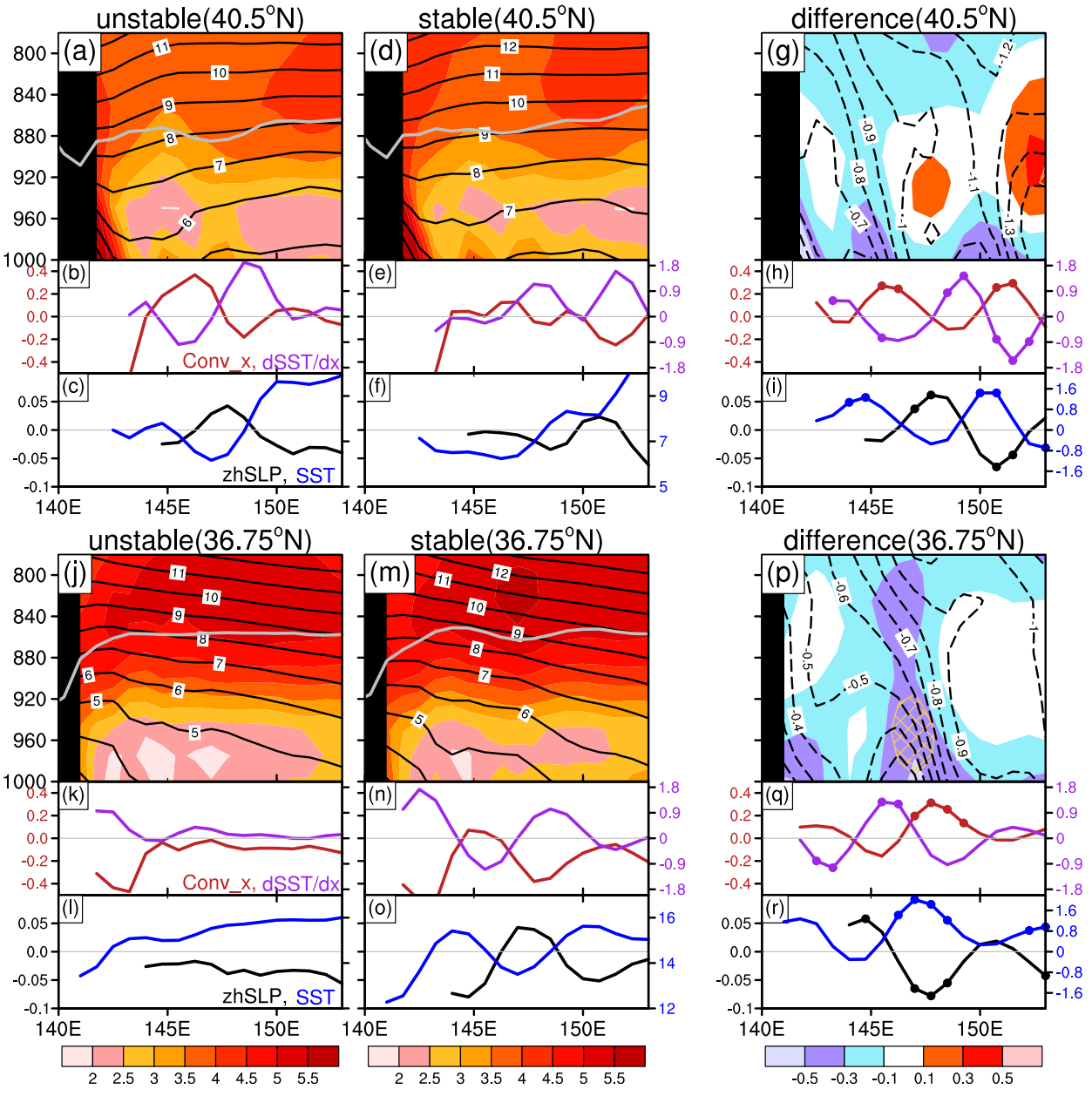

FIG. 13. (a) Winter-mean zonal cross section for 40.5°N of zonal wind (contoured every 1 m s^{-1}) and the vertical gradient du/dz (m s^{-1} km^{-1}; shaded as indicated at the bottom of the figure), with the MABL top (gray line), composited for the unstable KE regime on the basis of the ERA-Interim (2002–14). (b) The corresponding zonal profiles of zonal surface wind convergence (i.e., $-du_s/dx$ at the lowest model level; 10^{-5} s^{-1}; red line, left y axis), dSST/dx [°C (100 km)$^{-1}$; purple line, right y axis], and (c) zhSLP (hPa; black line, left y axis) and SST (°C; blue line, right y axis) (d)–(f) As in (a)–(c), but for the stable KE regime. (g)–(i) As in (a)–(c), but for the corresponding composited differences. In (h),(i), dots show where the differences are statistically significant at the 90% confidence level. (j)–(r) As in (a)–(i), but for 36.75°N. Orange hatched areas in (g),(p) show that the composited differences in du/dz are significant at the 90% confidence level.

$$\mathrm{LHF} = \rho_a L C_E W_a (q_s - q_a), \tag{2}$$

respectively. In (1) and (2), subscripts s and a signify quantities at the sea surface and in the air just above it, respectively, and $W = (u^2 + v^2)^{1/2}$ represents scalar wind speed with the zonal u and meridional v wind velocities. The transfer coefficients of heat and moisture are denoted by C_H and C_E, respectively; C_p is the specific heat of dry air at constant pressure; L is the latent heat of vaporization; T is temperature; q is specific humidity; and ρ is air density. If

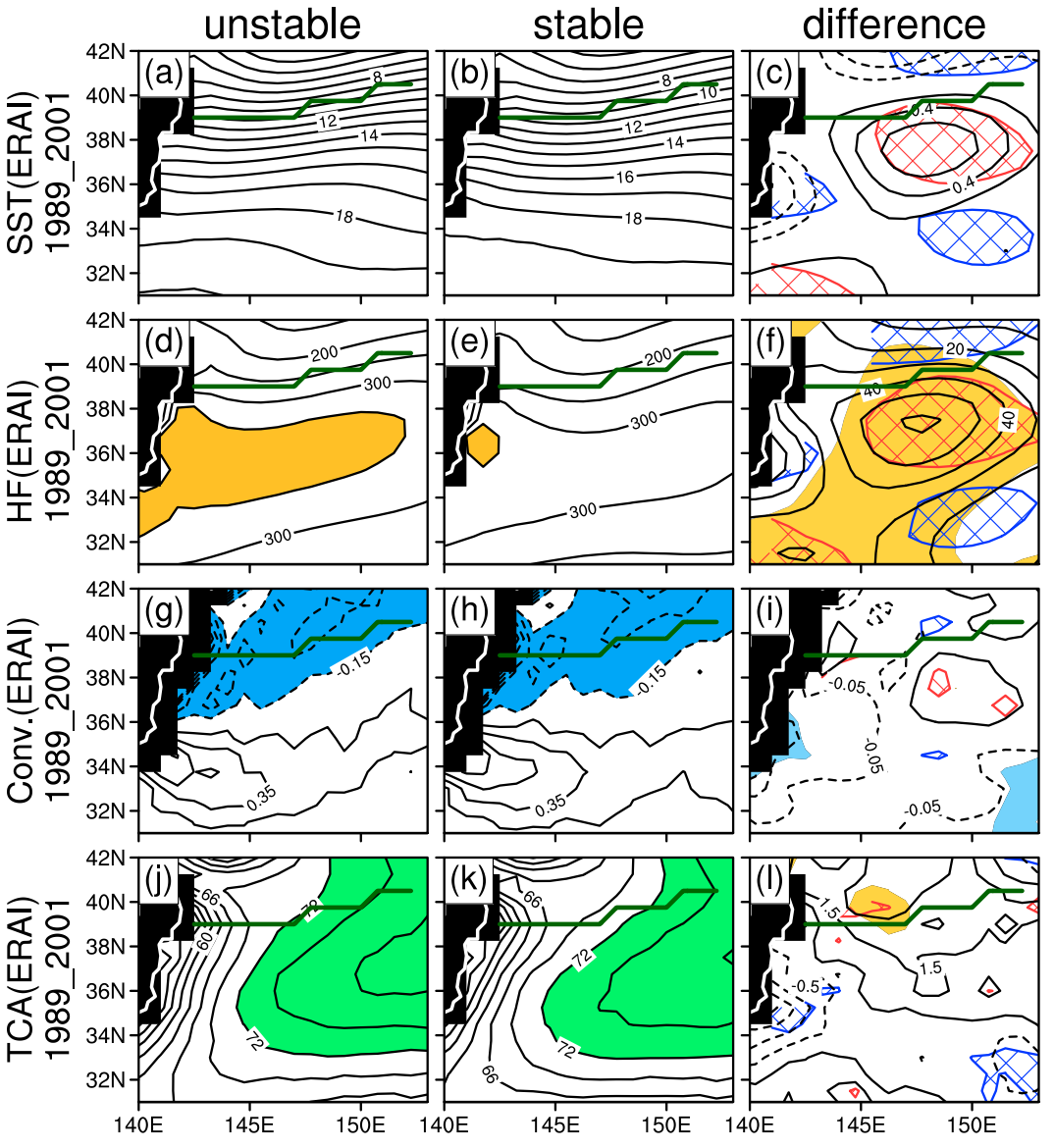

FIG. 14. As in Fig. 9, but for the LR period (1989–2001) of the ERA-Interim. (a),(b) SST (contoured every 1°C) and (c) its difference (contoured every 0.2°C; zero line are omitted). (d),(e) SHF + LHF (contoured every 50 W m^{-2}; shaded in yellow where its values exceed 350 W m^{-2}) and (f) the difference (contoured every 10 W m^{-2}). (g),(h) Surface wind convergence (contoured at intervals of 0.2×10^{-5} s^{-1} starting from $\pm 0.15 \times 10^{-5}$ s^{-1}; dashed for divergence; shaded where its values are below -0.15×10^{-5} s^{-1}) and (i) the difference (contoured at intervals of 0.1×10^{-5} s^{-1} starting from $\pm 0.05 \times 10^{-5}$ s^{-1}; dashed for negative). (j),(k) TCA (contoured every 3%; shaded where its values exceed 72%) and (l) the difference (contoured at intervals of 1% starting from ±0.5%). Green lines indicate SST fronts where equatorward gradients in SST prescribed for the ERA-Interim in the LR period maximizes.

fluctuations in ρ, C_H, and C_E are assumed to be negligible, wintertime-mean SHF and LHF may be linearized as

$$\langle \mathrm{SHF} \rangle = \rho_a C_p C_H [\overline{\overline{W_a}}\,(\overline{\overline{T_s}} - \overline{\overline{T_a}}) + \overline{\overline{W_a}}\,\langle T_s' \rangle - \overline{\overline{W_a}}\,\langle T_a' \rangle + \langle W_a' \rangle (\overline{\overline{T_s}} - \overline{\overline{T_a}}) + (\langle W_a' T_s' \rangle - \langle W_a' T_a' \rangle)] \tag{3}$$

and

$$\langle \mathrm{LHF} \rangle = \rho_a L C_E [\overline{\overline{W_a}}\,(\overline{\overline{q_s}} - \overline{\overline{q_a}}) + \overline{\overline{W_a}}\,\langle q_s' \rangle - \overline{\overline{W_a}}\,\langle q_a' \rangle + \langle W_a' \rangle (\overline{\overline{q_s}} - \overline{\overline{q_a}}) + (\langle W_a' q_s' \rangle - \langle W_a' q_a' \rangle)], \tag{4}$$

where double overbars and primes indicate wintertime climatologies and deviations from them, respectively, and angle brackets denote winter means. Note that the mean scalar wind speed is estimated locally as the time

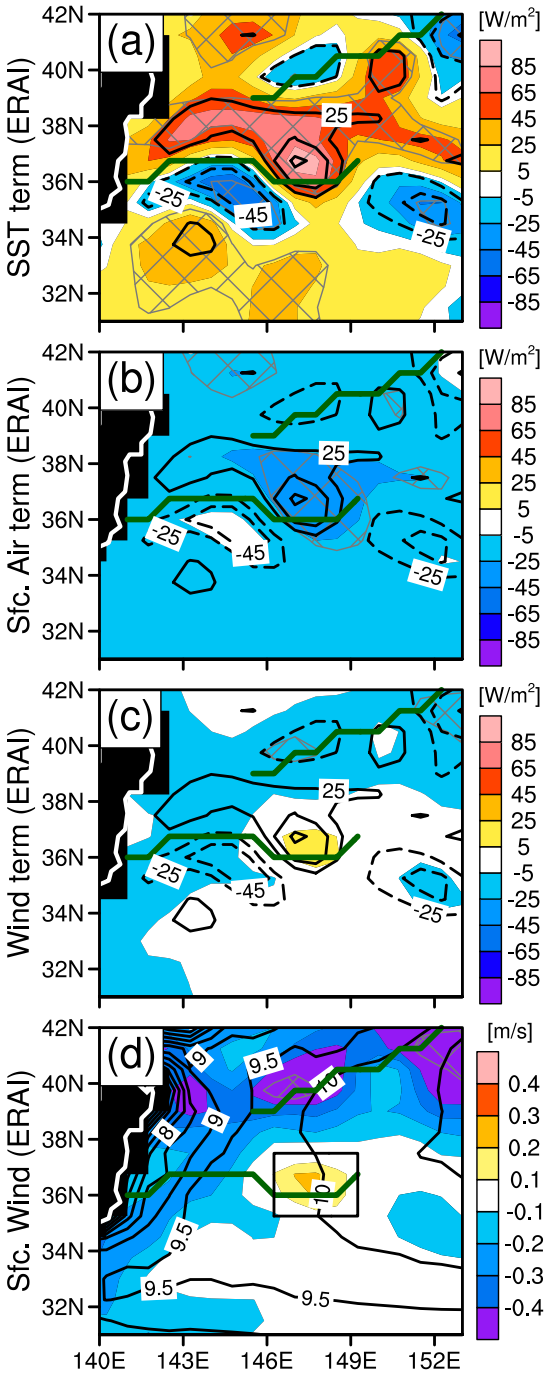

FIG. 15. (a) Wintertime (December–March) composited differences in SHF and LHF combined between the unstable and stable KE regimes for 2002–14 based on the ERA-Interim, estimated from all the terms of (3) and (4) for the linearized bulk aerodynamic formulas (contoured at intervals of 20 W m^{-2} from ±25 W m^{-2}) and those attributed to the SST term (W m^{-2}; shaded as indicated on the right). (b) As in (a), but for the contribution from the surface air term in place of the SST term. (c) As in (a), but for the contribution from the wind term. (d) Wintertime climatology of surface scalar wind speed (contoured every 0.5 m s^{-1}), and its composited difference (m s^{-1}; shaded as indicated on the right). Green lines indicate the axes of the KE and Oyashio fronts at which climatological-mean equatorward SST gradient maximizes locally.

average of daily scalar wind speeds based on the OAFlux data or the 6-hourly wind speeds based on the ERA-Interim data. Saturated specific humidity at the surface $q_{\rm sat}$ is estimated from SST (T_s in kelvin) as

$$q_{\rm sat} = 0.622\frac{6.112}{P_s}\exp\left(17.67\frac{T_s - 273.16}{T_s - 29.66}\right) \qquad (5)$$

(e.g., Bolton 1980; Stull 1988), where P_s (=1014.0 hPa) is surface pressure, which is estimated from the ERA-Interim climatology (2002–2014) for winter as an average over the KOE region (33.75°–41.25°N, 143.25°–150°E). For simplicity, we use typical values for the constants as $C_p = 1004\,{\rm J\,K^{-1}\,kg^{-1}}$, $L = 2.5\times10^6\,{\rm J\,kg^{-1}}$, $C_H = C_E = 1.5\times10^{-6}$, and $\rho_a = 1.225\,{\rm kg\,m^{-3}}$ (e.g., Arya 2001). We have confirmed that the composites of SHF and LHF combined for the unstable and stable KE regimes estimated from all the terms in (3) and (4) are quite similar to those estimated from heat fluxes as outputs of the OAFlux and ERA-Interim, only with slight overestimations.

The sum of the second terms in (3) and (4) can be considered as direct contributions from SST anomalies (SST term) to the total flux anomalies. Likewise, the sum of the third terms in (3) and (4), which are proportional to anomalies in SAT and specific humidity, are considered as the contribution from anomalous surface air conditions (surface air term), whereas the sum of the fourth terms are considered as the direct contribution from surface wind speed anomalies (wind term). The other terms related to covariance between anomalies are found negligible (not shown).

Figure 15a shows composited differences in the ERA-Interim surface heat fluxes estimated from all the terms of (3) and (4) (contoured), superimposed on those only from the SST term (shaded). The SST term accounts for +140% of the total heat fluxes anomalies (i.e., overestimation), which are partially offset by the surface air term (about −50%) (Fig. 15b). The wind term makes a slight positive contribution (about +7%) only over the strongest SST anomalies (Fig. 15c), where the surface wind speed locally intensifies (Fig. 15d), although the local enhancement of the wind term and the wind speed itself is not statistically significant. These budgets are overall consistent with the corresponding evaluation based on the OAFlux (2002–14), only with slight differences in their amplitude (+95% for the SST term, −15% for the surface air term, and +15% for the wind term) and significant anomalies in wind speed. As indicated by its composited vertical profiles (Fig. 16a), the scalar wind speed in the free troposphere is weaker over the strongest positive SST anomalies in the unstable KE regime, but it strengthens near the surface. Although

not statistically significant, the vertical wind shear in MABL is weaker in the unstable regime (Fig. 16b). The reduced wind shear can be due to enhanced momentum mixing over the particularly warm SST anomaly through modulating MABL stability (Liu et al. 2013).

The same analysis as above was repeated for 1989–2014 but on the basis of the OAFlux data. The wind term is found to account for as much as +30% of total heat flux anomalies because of statistically significant local enhancement of surface scalar wind speed over the positive SST anomalies, despite the tendency for the wind speed in the free troposphere to be weaker in the unstable KE regime than in stable KE regime (not shown), as is the case for the period 2002–14. The SST term still accounts for more than 65% of the anomalous heat fluxes. In agreement with Sugimoto and Hanawa (2011), the results above indicate that SST anomalies play a dominant role in determining heat flux anomalies primarily through modulating temperature and humidity difference between sea surface and surface atmosphere and through secondary effect by modulating surface wind speed.

6. Maintenance of near-surface baroclinic zones modulated by KE variability

Masunaga et al. (2015) investigated the formation and/or maintenance of dual near-surface baroclinic zones observed within the wintertime KOE region. Acting against the relaxing effect by transient eddies, the climatological reinforcement of meridional SAT gradient evaluated with a frontogenetical function is primarily through meridional contrasts in SHF across the Oyashio front and through the confluence of the monsoonal northerlies into the pressure trough maintained mainly through the hydrostatic effect near the warm KE.

Figure 17 shows how each of these frontogenetical processes evaluated through the formulas derived in the appendix tends to be modulated in association with the KE variability. As in the climatology, the surface baroclinic zone along the Oyashio front is maintained primarily through the cross-frontal SHF contrast in both the stable and unstable KE regimes (Figs. 17a,b), although the SHF contrast is enhanced in the unstable regime because of the warming in the mixed water region. In the stable KE regime, a contribution from the SHF contrast is positive across the SST front along the intensified KE jet (Fig. 17b), while the contribution is negative (i.e., frontolysis) in the unstable regime (Fig. 17a). Monthly mean meridional wind confluence contributes positively to the maintenance of the baroclinic zone along the KE jet in each of its stable and unstable regimes (Figs. 17d,e), and the particular contribution is somewhat stronger in the stable regime (Figs. 17e,f).

These frontogenetical contributions as thermal influence from the ocean are counteracted by the meridional thermal advection by atmospheric transient eddies (Figs. 17g–i), which is enhanced along the KE front in the stable regime and along the Oyashio front in the unstable KE regime in a manner consistent with stronger SST gradients. In fact, meridional temperature gradient at the 975-hPa level along the mean KE front is significantly stronger in the stable KE regime than in the unstable regime (Figs. 17j–l). Although not statistically significant, the strengthening of baroclinicity is observed throughout the depth of the MABL, leading to the enhancement of the Eady growth rate at the 850-hPa level in the stable KE regime (not shown). On the contrary, Révelard et al. (2016) found the reduction of the Eady growth rate in October through January during the stable KE regime, through a lag-regression analysis (KEI leads) applied to the ERA-Interim for the period of 1979–2012. This discrepancy may be attributable to the possible seasonality and/or artificially smoothed SST prescribed for the ERA-Interim in the LR period (1979–2001), which has been excluded from our analysis. In fact, unlike in our analysis (Fig. 4), their statistics show no significant SST anomalies in the mixed water region (e.g., their Fig. 5a). Still, it remains for future study to elucidate how the KE regime shifts can modulate the development of synoptic-scale atmospheric disturbances through modifying surface baroclinic zones within the KOE region.

7. Summary and concluding remarks

The present study has clearly identified local mesoscale influence of the KE variability on MABL on the basis of the KE index proposed by Qiu et al. (2014). As pointed out by previous studies (Sugimoto and Hanawa 2011; Sasaki and Minobe 2015), SST in the mixed water region is higher than its climatology in the unstable KE regime, owing to warm oceanic eddies frequently shed from the meandering KE jet. The SST gradient across the KE front is thus weaker, while it is stronger across the Oyashio front to the north. In the stable KE regime, by contrast, SST in the mixed water region is lower, while the KE jet, the cross-frontal SST gradient and associated surface baroclinic zones are all stronger. Since the late 1980s, the KE regime shifts have been the dominant factor in controlling mesoscale SST variability within the KOE region.

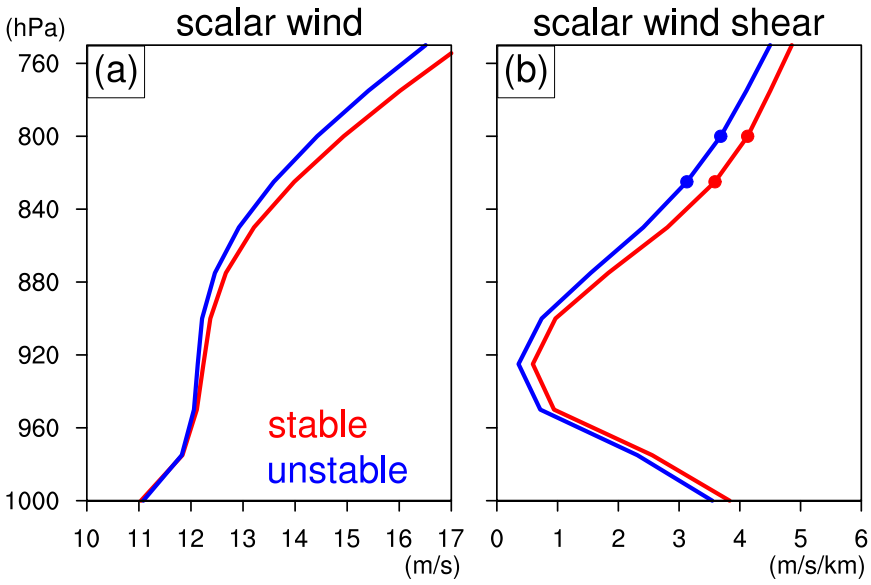

FIG. 16. (a) Vertical profiles of wintertime (December–March) scalar wind speed based on the ERA-Interim (2002–14) composited separately of for the unstable (blue) and stable (red) KE regimes, based on the average over 35.25°–37.5°N, 146.25°–149.25°E (rectangular domain indicated in Fig. 15d). (b) As in (a), but for the vertical gradient of the scalar wind ($m\ s^{-1}\ km^{-1}$). Dots denote the composited differences that are statistically significant at the 90% confidence level.

Satellite-based observational data show that, in the unstable KE regime, a domain of enhanced cloudiness and turbulent heat fluxes from the ocean is broadened meridionally into the warmed mixed water region, while in the stable regime the domain is elongated zonally but confined meridionally into the intensified KE jet. The enhancement (reduction) of cloudiness and heat fluxes occurs over positive (negative) anomalies in both SST and surface wind convergence over the mixed water region. On the basis of the ERA-Interim atmospheric reanalysis in its high-resolution SST period since 2002, we have shown that those positive anomalies in the unstable KE regime coincide with the locally warmer MABL and a cyclonic (meridionally high-pass filtered) SLP anomaly, and vice versa in the stable KE regime. The mesoscale SLP anomaly can indeed consistent with temperature anomalies in the MABL through hydrostatic relation. As hinted in satellite data as a slight enhancement of precipitation in the unstable KE regime, the ERA-Interim suggests significant enhancement of convective precipitation over the warmed mixed water region, although this result should be viewed with caution since precipitation from the data of an atmospheric reanalysis is sensitive to the parameterization of its forecast model. These results nevertheless suggest that mesoscale SST variability associated with the KE regime changes can leave distinct imprints on the overlying MABL primarily through the ''hydrostatic effect.'' The results also imply the distinct dual-peak mesoscale profiles of atmospheric variables within the MABL observed in the 11-yr mean fields from 2002 to 2012 by Masunaga et al. (2015) are representative of the stable KE regime that occupied 7 out of the 11 years. Our close examination of zonal sections suggests that local SST anomalies can modulate surface winds through modulating not only the hydrostatic effect but also static stability in MABL, known as the ''vertical mixing effect.'' It will be examined in a future study how the relative importance between the two processes varies with the KE variability to modify near-surface wind distribution.

The present study has also verified that the aforementioned modulations in mesoscale features in MABL associated with the KE regime changes are not well represented in the ERA-Interim during its LR period. The improved representation of surface winds may be attributable in part to satellite scatterometer measurements of sea surface winds (i.e., QuikSCAT; Dee et al. 2011) assimilated into the ERA-Interim in the HR period. Still, the present study, as well as Chelton (2005) and Masunaga et al. (2015), highlights the importance of high-resolution SST prescribed for the atmospheric

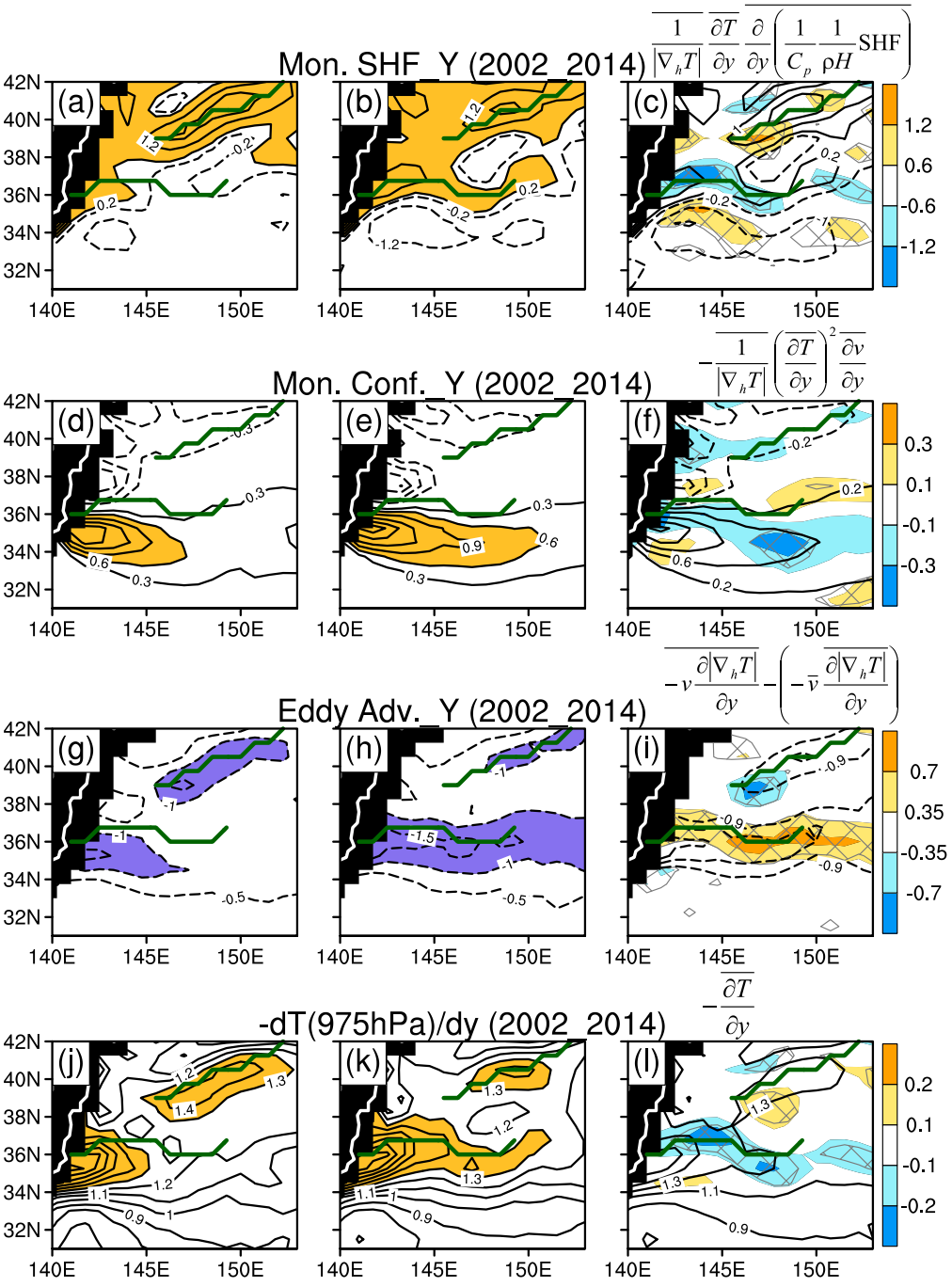

FIG. 17. (a)–(i) Wintertime composite maps of the dominant terms in frontogenetical function [K (100 km)$^{-1}$ day^{-1}] evaluated at 975 hPa. Contribution from monthly mean meridional SHF gradient ∂SHF/∂y (contoured at intervals of 1 from $\pm$0.2; dashed for frontolysis; shaded in yellow where its values exceed +0.2) for the (a) unstable and (b) stable KE regimes and (c) the differences (shaded as indicated to the right) and wintertime climatology of ∂SHF/∂y (contoured at intervals of 0.8 starting from $\pm$0.2; dashed for frontolysis). Hatched areas where the difference is significant at the 90% confidence level. (d),(e) As in (a),(b), but for monthly mean meridional confluence term (contoured every 0.3; zero lines are omitted; shaded in yellow where its values exceed +0.6). (f) As in (c), but for the meridional confluence term (contoured at intervals of 0.4 starting from $\pm$0.2). (g),(h) As in (a),(b), but for meridional advection by transient eddies (contoured every 0.5; dashed for frontolysis; shaded in purple where its values are below $-$1.0). (i) As in (c), but for the meridional advection by transient eddies (contoured at intervals of 0.3 starting from $\pm$0.9). (j),(k) As in (a),(b), but meridional air temperature gradients at 975 hPa (contoured at intervals of 0.1; shaded in yellow where its values exceed +1.3). (l) As in (c), but for the meridional air temperature gradients at 975 hPa (contoured at intervals of 0.2). Green lines indicate the KE and Oyashio fronts at which climatological-mean meridional SST gradient maximizes locally.

reanalysis for better representation of mesoscale features in MABL.

Sugimoto (2014) showed that SSTs in the western (36°–40°N, 143°–148°E) and eastern (36°–40°N, 155°–160°E) portions of the KOE region tend to vary rather independently. Our composite analysis indicates that, in the unstable KE regime, weaker but significant negative anomalies in SST and upward heat fluxes are observed in the eastern portion, as opposed to the western portion (not shown). Although convective precipitation significantly weakens over the negative SST anomaly, no other significant signals, including surface wind convergence, can be found in the MABL over the eastern portion. These characteristics seem consistent with those briefly described by Révelard et al. (2016). It still remains for a future study to reveal the detailed local oceanic influence on the overlying atmosphere in the eastern KOE region.

The results in the present study are based on a limited number of years, and therefore the statistics obtained may lack enough robustness because of sampling fluctuations. In particular, the statistical significance of the composite anomalies for the unstable regime in the HR period seems rather sensitive to sampling fluctuations. Still, the composited anomalies in the mixed water region barely exceed the 90% confidence level if the data for the 2009 winter is excluded (not shown). Likewise, the lack of statistically significant anomalies in the ERA-Interim in its LR period (Fig. 14) might be attributed in part to the smallness of degrees of freedom. Therefore the robustness of the above results must be verified in future based on a longer dataset, for example, through comparing two additional products of the new Japanese reanalysis of the global atmosphere (JRA-55; Kobayashi et al. 2015): one with high-resolution (0.25° × 0.25°) SST and the other with low-resolution (1.0° × 1.0°) SST prescribed for the same data assimilation system.

Acknowledgments. We thank Professors Ping Chang and Niklas Schneider for their valuable comments. We also thank two anonymous reviewers for their useful and constructive comments that have led our paper to its substantial improvement. This study is supported in part by the Japanese Ministry of Education, Culture, Sports Science and Technology (MEXT) through Grants-in-Aid for Scientific Research 2205, 2409 (in Innovative Areas), and 25287120 and also by the Japanese Ministry of Environment through the Environment Research and Technology Department Funds 2A1201 and 2-1503. BQ acknowledges support from NASA Grant NNX13AE51G.

APPENDIX

Frontogenetical Function

For the sake of convenience, the frontogenetical function F provided by Masunaga et al. (2015) is recapitulated in the following:

$$F \equiv \frac{d}{dt}|\nabla_h T| = -\frac{1}{|\nabla_h T|}\left[\left(\frac{\partial T}{\partial x}\right)^2\frac{\partial u}{\partial x} + \left(\frac{\partial T}{\partial y}\right)^2\frac{\partial v}{\partial y}\right] \tag{A1a}$$

$$-\frac{1}{|\nabla_h T|}\frac{\partial T}{\partial x}\frac{\partial T}{\partial y}\left(\frac{\partial v}{\partial x}+\frac{\partial u}{\partial y}\right) \tag{A1b}$$

$$-\frac{1}{|\nabla_h T|}\frac{\partial T}{\partial p}\left(\frac{\partial T}{\partial x}\frac{\partial \omega}{\partial x}+\frac{\partial T}{\partial y}\frac{\partial \omega}{\partial y}\right) \tag{A1c}$$

$$+\frac{1}{|\nabla_h T|}\left[\frac{\partial T}{\partial x}\frac{\partial}{\partial x}\left(\frac{1}{C_p}\frac{RT}{p}\omega\right) + \frac{\partial T}{\partial y}\frac{\partial}{\partial y}\left(\frac{1}{C_p}\frac{RT}{p}\omega\right)\right] \tag{A1d}$$

$$+\frac{1}{|\nabla_h T|}\left[\frac{\partial T}{\partial x}\frac{\partial}{\partial x}\left(\frac{1}{C_p}\frac{1}{\rho H}\mathrm{SHF}\right) + \frac{\partial T}{\partial y}\frac{\partial}{\partial y}\left(\frac{1}{C_p}\frac{1}{\rho H}\mathrm{SHF}\right)\right] \tag{A1e}$$

$$+\mathrm{Residual}. \tag{A1f}$$

In (A1), ω denotes vertical pressure velocity at a given pressure level, H the depth of the convective boundary layer, and R the gas constant of dry air; and other notations are the same as in (1). Here, ρ may be considered as air density vertically averaged within the boundary layer. In the present study, we use constant values of $R = 287\,\mathrm{J\,K^{-1}\,kg^{-1}}$, $H = 1200\,\mathrm{m}$, and $\rho = 1\,\mathrm{kg\,m^{-3}}$. For simplicity, H and ρ are assumed to be uniform in space.

The first and second terms in each line of (A1), if positive, act to strengthen zonal and meridional gradients of T. The first [(A1a)], second [(A1b)], and third [(A1c)] lines on the rhs of (A1) are called confluence, shear, and tilting terms, respectively. The fourth [(A1d)] and fifth [(A1e)] lines represent contributions from adiabatic volume change and diabatic heating through SHF, respectively. The residual term [(A1f)] can be estimated by assuming a steady state $\overline{\partial|\nabla_h T|/\partial t} = 0$. Each term of (A1) can then be decomposed into contributions from monthly mean circulation and submonthly transients. For example, the former contribution to the zonal confluence term may be expressed as

$$-\overline{\frac{1}{|\nabla_h T|}}\left(\overline{\frac{\partial T}{\partial x}}\right)^2\overline{\frac{\partial u}{\partial x}},$$

where the single overbar signifies monthly mean quantities. The contribution from submonthly transients can be obtained, for example, as

$$-\overline{\frac{1}{|\nabla_h T|}\left(\frac{\partial T}{\partial x}\right)^2\frac{\partial u}{\partial x}}-\left[-\frac{1}{|\nabla_h T|}\left(\frac{\partial \overline{T}}{\partial x}\right)^2\frac{\partial \overline{u}}{\partial x}\right],$$

where the first term has been evaluated from 6-hourly data.

REFERENCES

Arya, S. P., 2001: *Introduction to Micrometeorology*. 2nd ed. International Geophysics Series, Vol. 79, Academic Press, 420 pp.

Bolton, D., 1980: The computation of equivalent potential temperature. *Mon. Wea. Rev.*, **108**, 1046–1053, doi:10.1175/1520-0493(1980)108<1046:TCOEPT>2.0.CO;2.

Chelton, D. B., 2005: The impact of SST specification on ECMWF surface wind stress fields in the eastern tropical Pacific. *J. Climate*, **18**, 530–550, doi:10.1175/JCLI-3275.1.

——, M. G. Schlax, M. H. Freilich, and R. F. Milliff, 2004: Satellite measurements reveal persistent small-scale features in ocean winds. *Science*, **303**, 978–983, doi:10.1126/science.1091901.

Dee, D. P., and Coauthors, 2011: The ERA-Interim reanalysis: Configuration and performance of the data assimilation system. *Quart. J. Roy. Meteor. Soc.*, **137**, 553–597, doi:10.1002/qj.828.

Ducet, N., P.-Y. Le Traon, and G. Reverdin, 2000: Global high-resolution mapping of ocean circulation from TOPEX/Poseidon and *ERS-1* and *-2*. *J. Geophys. Res.*, **105**, 19 477–19 498, doi:10.1029/2000JC900063.

Fairall, C. W., E. F. Bradley, J. E. Hare, A. A. Grachev, and J. B. Edson, 2003: Bulk parameterization of air–sea fluxes: Updates and verification for the COARE algorithm. *J. Climate*, **16**, 571–591, doi:10.1175/1520-0442(2003)016<0571:BPOASF>2.0.CO;2.

Frankignoul, C., N. Sennechael, Y.-O. Kwon, and M. A. Alexander, 2011: Influence of the meridional shifts of the Kuroshio and the Oyashio Extensions on the atmospheric circulation. *J. Climate*, **24**, 762–777, doi:10.1175/2010JCLI3731.1.

Frenger, I., N. Gruber, R. Knutti, and M. Münnich, 2013: Imprint of Southern Ocean eddies on winds, clouds and rainfall. *Nat. Geosci.*, **6**, 608–612, doi:10.1038/ngeo1863.

Hayes, S. P., M. J. McPhaden, and J. M. Wallace, 1989: The influence of sea surface temperature on surface wind in the eastern equatorial Pacific: Weekly to monthly variability. *J. Climate*, **2**, 1500–1506, doi:10.1175/1520-0442(1989)002<1500:TIOSST>2.0.CO;2.

Hotta, D., and H. Nakamura, 2011: On the significance of sensible heat supply from the ocean in the maintenance of mean baroclinicity along storm tracks. *J. Climate*, **24**, 3377–3401, doi:10.1175/2010JCLI3910.1.

Hubanks, P. A., M. D. King, S. A. Platnick, and R. A. Pincus, 2008: MODIS Atmosphere L3 gridded product algorithm theoretical basis document. MODIS Tech. Doc. ATBD-MOD-30, 96 pp. [Available online at http://modis-atmos.gsfc.nasa.gov/_docs/L3_ATBD_2008_12_04.pdf.]

Iizuka, S., 2010: Simulations of wintertime precipitation in the vicinity of Japan: Sensitivity to fine-scale distributions of SST. *J. Geophys. Res.*, **115**, D10107, doi:10.1029/2009JD012576.

Isoguchi, O., H. Kawamura, and E. Oka, 2006: Quasi-stationary jets transporting surface warm waters across the transition zone between the subtropical and the subarctic gyres in the North Pacific. *J. Geophys. Res.*, **111**, C10003, doi:10.1029/2005JC003402.

Kalnay, E., and Coauthors, 1996: The NCEP/NCAR 40-Year Reanalysis Project. *Bull. Amer. Meteor. Soc.*, **77**, 437–471, doi:10.1175/1520-0477(1996)077<0437:TNYRP>2.0.CO;2.

Kanamitsu, M., W. Ebisuzaki, J. Woollen, S.-K. Yang, J. J. Hnilo, M. Fiorino, and G. L. Potter, 2002: NCEP–DOE AMIP-II Reanalysis (R-2). *Bull. Amer. Meteor. Soc.*, **83**, 1631–1643, doi:10.1175/BAMS-83-11-1631.

Kawai, H., 1972: Hydrography of the Kuroshio Extension. *Kuroshio: Its Physical Aspects*, H. Stommel and K. Yoshida, Eds., University of Tokyo Press, 235–352.

Kelly, K. A., R. J. Small, R. M. Samelson, B. Qiu, T. M. Joyce, Y.-O. Kwon, and M. F. Cronin, 2010: Western boundary currents and frontal air–sea interaction: Gulf Stream and Kuroshio Extension. *J. Climate*, **23**, 5644–5667, doi:10.1175/2010JCLI3346.1.

Kida, S., and Coauthors, 2015: Oceanic fronts and jets around Japan: A review. *J. Oceanogr.*, **71**, 469–497, doi:10.1007/s10872-015-0283-7.

Kilpatrick, T., N. Schneider, and B. Qiu, 2014: Boundary layer convergence induced by strong winds across a mid-latitude SST front. *J. Climate*, **27**, 1698–1718, doi:10.1175/JCLI-D-13-00101.1.

Kobayashi, S., and Coauthors, 2015: The JRA-55 Reanalysis: General specifications and basic characteristics. *J. Meteor. Soc. Japan*, **93**, 5–48, doi:10.2151/jmsj.2015-001.

Kubota, M., and H. Tomita, 2007: Present state of the J-OFURO air–sea interaction data product. Flux News, No. 4, WCRP Working Group on Surface Fluxes, Southampton, United Kingdom, 13–15.

Kwon, Y.-O., M. Alexander, N. Bond, C. Frankignoul, H. Nakamura, B. Qiu, and L. Thompson, 2010: Role of the Gulf Stream and Kuroshio–Oyashio systems in large-scale atmosphere–ocean interaction: A review. *J. Climate*, **23**, 3249–3281, doi:10.1175/2010JCLI3343.1.

Lindzen, R. S., and S. Nigam, 1987: On the role of sea surface temperature gradients in forcing low-level winds and convergence in the tropics. *J. Atmos. Sci.*, **44**, 2418–2436, doi:10.1175/1520-0469(1987)044<2418:OTROSS>2.0.CO;2.

Liu, J.-W., S.-P. Zhang, and S.-P. Xie, 2013: Two types of surface wind response to the East China Sea Kuroshio front. *J. Climate*, **26**, 8616–8627, doi:10.1175/JCLI-D-12-00092.1.

Masunaga, R., H. Nakamura, T. Miyasaka, K. Nishii, and Y. Tanimoto, 2015: Separation of climatological imprints of the Kuroshio Extension and Oyashio fronts on the wintertime atmospheric boundary layer: Their sensitivity to SST resolution prescribed for atmospheric reanalysis. *J. Climate*, **28**, 1764–1787, doi:10.1175/JCLI-D-14-00314.1.

Minobe, S., A. Kuwano-Yoshida, N. Komori, S.-P. Xie, and R. J. Small, 2008: Influence of the Gulf Stream on the troposphere. *Nature*, **452**, 206–209, doi:10.1038/nature06690.

——, M. Miyashita, A. Kuwano-Yoshida, H. Tokinaga, and S.-P. Xie, 2010: Atmospheric response to the Gulf Stream: Seasonal variations. *J. Climate*, **23**, 3699–3719, doi:10.1175/2010JCLI3359.1.

Miyasaka, T., H. Nakamura, B. Taguchi, and M. Nonaka, 2014: Multidecadal modulations of the low-frequency climate variability in the wintertime North Pacific since 1950. *Geophys. Res. Lett.*, **41**, 2948–2955, doi:10.1002/2014GL059696.

Nakamura, H., and A. S. Kazmin, 2003: Decadal changes in the North Pacific oceanic frontal zones as revealed in ship and satellite observations. *J. Geophys. Res.*, **108**, 3078–3094, doi:10.1029/1999JC000085.

——, G. Lim, and T. Yamagata, 1997: Decadal climate variability in the North Pacific during the recent decades. *Bull. Amer. Meteor. Soc.*, **78**, 2215–2225, doi:10.1175/1520-0477(1997)078<2215:DCVITN>2.0.CO;2.

——, T. Sampe, Y. Tanimoto, and A. Shimpo, 2004: Observed associations among storm tracks, jet streams and midlatitude oceanic fronts. *Earth's Climate: The Ocean–Atmosphere Interaction*, *Geophys. Monogr.*, Vol. 147, Amer. Geophys. Union, 329–345.

——, ——, A. Goto, W. Ohfuchi, and S.-P. Xie, 2008: On the importance of midlatitude oceanic frontal zones for the mean state and dominant variability in the tropospheric circulation. *Geophys. Res. Lett.*, **35**, L15709, doi:10.1029/2008GL034010.

Nonaka, M., and S.-P. Xie, 2003: Covariations of sea surface temperature and wind over the Kuroshio and its extension: Evidence for ocean-to-atmosphere feedback. *J. Climate*, **16**, 1404–1413, doi:10.1175/1520-0442(2003)16<1404:COSSTA>2.0.CO;2.

——, H. Nakamura, Y. Tanimoto, T. Kagimoto, and H. Sasaki, 2006: Decadal variability in the Kuroshio–Oyashio Extension simulated in an eddy-resolving OGCM. *J. Climate*, **19**, 1970–1989, doi:10.1175/JCLI3793.1.

O'Neill, L. W., S. K. Esbensen, N. Thum, R. M. Samelson, and D. B. Chelton, 2010: Dynamical analysis of the boundary layer and surface wind responses to mesoscale SST perturbations. *J. Climate*, **23**, 559–581, doi:10.1175/2009JCLI2662.1.

O'Reilly, C. H., and A. Czaja, 2015: The response of the Pacific storm track and atmospheric circulation to Kuroshio Extension variability. *Quart. J. Roy. Meteor. Soc.*, **141**, 52–66, doi:10.1002/qj.2334.

Perry, K. L., 2001: SeaWinds on QuikSCAT level 3 daily, gridded ocean wind vectors (JPL SeaWinds project) version 1.1. JPL Doc. D-20335, Jet Propulsion Laboratory, Pasadena, CA, 39 pp. [Available online at http://podaac.jpl.nasa.gov.]

Qiu, B., 2003: Kuroshio Extension variability and forcing of the Pacific decadal oscillations: Responses and potential feedback. *J. Phys. Oceanogr.*, **33**, 2465–2482, doi:10.1175/2459.1.

——, and S. Chen, 2005: Variability of the Kuroshio Extension jet, recirculation gyre, and mesoscale eddies on decadal time scales. *J. Phys. Oceanogr.*, **35**, 2090–2103, doi:10.1175/JPO2807.1.

——, and ——, 2010: Eddy-mean flow interaction in the decadally modulating Kuroshio Extension system. *Deep-Sea Res. II*, **57**, 1098–1110, doi:10.1016/j.dsr2.2008.11.036.

——, ——, N. Schneider, and B. Taguchi, 2014: A coupled decadal prediction of the dynamic state of the Kuroshio Extension system. *J. Climate*, **27**, 1751–1764, doi:10.1175/JCLI-D-13-00318.1.

Révelard, A., C. Frankignoul, N. Sennéchael, Y.-O. Kwon, and B. Qiu, 2016: Influence of the decadal variability of the Kuroshio Extension on the atmospheric circulation in the cold season. *J. Climate*, doi:10.1175/JCLI-D-15-0511.1, in press.

Reynolds, R. W., T. M. Smith, C. Liu, D. B. Chelton, K. S. Casey, and M. G. Schlax, 2007: Daily high-resolution-blended analyses for sea surface temperature. *J. Climate*, **20**, 5473–5496, doi:10.1175/2007JCLI1824.1.

Sampe, T., H. Nakamura, A. Goto, and W. Ohfuchi, 2010: Significance of a midlatitude SST frontal zone in the formation of a storm track and an eddy-driven westerly jet. *J. Climate*, **23**, 1793–1814, doi:10.1175/2009JCLI3163.1.

Sasaki, H., M. Nonaka, Y. Masumoto, Y. Sasai, H. Uehara, and H. Sakuma, 2008: An eddy-resolving hindcast simulation of the quasiglobal ocean from 1950 to 2003 on the Earth simulator. *High Resolution Numerical Modelling of the Atmosphere and Ocean*, K. Hamilton and W. Ohfuchi, Eds., Springer, 157–185.

Sasaki, Y. N., and S. Minobe, 2015: Climatological mean features and interannual to decadal variability of ring formations in the Kuroshio Extension region. *J. Oceanogr.*, **71**, 499–509, doi:10.1007/s10872-014-0270-4.

——, ——, and N. Schneider, 2013: Decadal response of the Kuroshio Extension jet to Rossby waves: Observation and thin-jet theory. *J. Phys. Oceanogr.*, **43**, 442–456, doi:10.1175/JPO-D-12-096.1.

Schneider, N., and B. Qiu, 2015: The atmospheric response to weak sea surface temperature fronts. *J. Atmos. Sci.*, **72**, 3356–3377, doi:10.1175/JAS-D-14-0212.1.

——, A. J. Miller, and D. W. Pierce, 2002: Anatomy of North Pacific decadal variability. *J. Climate*, **15**, 586–605, doi:10.1175/1520-0442(2002)015<0586:AONPDV>2.0.CO;2.

Seager, R., Y. Kushnir, N. H. Naik, M. A. Cane, and J. Miller, 2001: Wind-driven shifts in the latitude of the Kuroshio–Oyashio Extension and generation of SST anomalies on decadal timescales. *J. Climate*, **14**, 4249–4265, doi:10.1175/1520-0442(2001)014<4249:WDSITL>2.0.CO;2.

Seo, Y., S. Sugimoto, and K. Hanawa, 2014: Long-term variations of the Kuroshio Extension path in winter: Meridional movement and path state change. *J. Climate*, **27**, 5929–5940, doi:10.1175/JCLI-D-13-00641.1.

Shimada, T., and S. Minobe, 2011: Global analysis of the pressure adjustment mechanism over sea surface temperature fronts using AIRS/*Aqua* data. *Geophys. Res. Lett.*, **38**, L06704, doi:10.1029/2010GL046625.

Small, R. J., and Coauthors, 2008: Air–sea interaction over ocean fronts and eddies. *Dyn. Atmos. Oceans*, **45**, 274–319, doi:10.1016/j.dynatmoce.2008.01.001.

Smirnov, D., M. Newman, M. A. Alexander, Y.-O. Kwon, and C. Frankignoul, 2015: Investigating the local atmospheric response to a realistic shift in the Oyashio sea surface temperature front. *J. Climate*, **28**, 1126–1147, doi:10.1175/JCLI-D-14-00285.1.

Song, Q., D. B. Chelton, S. K. Esbensen, N. Thum, and L. W. O'Neill, 2009: Coupling between sea surface temperature and low-level winds in mesoscale numerical models. *J. Climate*, **22**, 146–164, doi:10.1175/2008JCLI2488.1.

Stull, R. B., 1988: *An Introduction to Boundary Layer Meteorology*. Atmospheric Sciences Library, Vol. 13, Kluwer Academic Publishers, 666 pp.

Sugimoto, S., 2014: Influence of SST anomalies on winter turbulent heat fluxes in the eastern Kuroshio–Oyashio confluence region. *J. Climate*, **27**, 9349–9358, doi:10.1175/JCLI-D-14-00195.1.

——, and K. Hanawa, 2011: Roles of SST anomalies on the wintertime turbulent heat fluxes in the Kuroshio–Oyashio confluence region: Influences of warm eddies detached from the Kuroshio Extension. *J. Climate*, **24**, 6551–6561, doi:10.1175/2011JCLI4023.1.

Taguchi, B., S.-P. Xie, N. Schneider, M. Nonaka, H. Sasaki, and Y. Sasai, 2007: Decadal variability of the Kuroshio Extension: Observations and an eddy-resolving model hindcast. *J. Climate*, **20**, 2357–2377, doi:10.1175/JCLI4142.1.

——, H. Nakamura, M. Nonaka, and S.-P. Xie, 2009: Influences of the Kuroshio/Oyashio Extensions on air–sea heat exchanges

and storm-track activity as revealed in regional atmospheric model simulations for the 2003/4 cold season. *J. Climate*, **22**, 6536–6560, doi:10.1175/2009JCLI2910.1.

——, ——, ——, N. Komori, A. Kuwano-Yoshida, K. Takaya, and A. Goto, 2012: Seasonal evolutions of atmospheric response to decadal SST anomalies in the North Pacific subarctic frontal zone: Observations and a coupled model simulation. *J. Climate*, **25**, 111–139, doi:10.1175/JCLI-D-11-00046.1.

Tanimoto, Y., H. Nakamura, T. Kagimoto, and S. Yamane, 2003: An active role of extratropical sea surface temperature anomalies in determining anomalous turbulent heat flux. *J. Geophys. Res.*, **108**, 3304, doi:10.1029/2002JC001750.

——, T. Kanenari, H. Tokinaga, and S.-P. Xie, 2011: Sea level pressure minimum along the Kuroshio and its Extension. *J. Climate*, **24**, 4419–4433, doi:10.1175/2011JCLI4062.1.

Tokinaga, H., Y. Tanimoto, S.-P. Xie, T. Sampe, H. Tomita, and H. Ichikawa, 2009: Ocean frontal effects on the vertical development of clouds over the western North Pacific: In situ and satellite observations. *J. Climate*, **22**, 4241–4260, doi:10.1175/2009JCLI2763.1.

Uppala, S. M., and Coauthors, 2005: The ERA-40 Re-Analysis. *Quart. J. Roy. Meteor. Soc.*, **131**, 2961–3012, doi:10.1256/qj.04.176.

Wagawa, T., S. Ito, Y. Shimizu, S. Kakehi, and D. Ambe, 2014: Currents associated with the quasi-stationary jet separated from the Kuroshio Extension. *J. Phys. Oceanogr.*, **44**, 1636–1653, doi:10.1175/JPO-D-12-0192.1.

Wallace, J. M., T. P. Mitchell, and C. Deser, 1989: The influence of sea surface temperature on surface wind in the eastern equatorial Pacific: Seasonal and interannual variability. *J. Climate*, **2**, 1492–1499, doi:10.1175/1520-0442(1989)002<1492:TIOSST>2.0.CO;2.

Wang, Y., and T. Liu, 2016: Observational evidence of frontal-scale atmospheric responses to Kuroshio Extension variability. *J. Climate*, **29**, 9459–9472, doi:10.1175/JCLI-D-14-00829.1.

Wentz, F. J., T. Meissner, C. Gentemann, and M. Brewer, 2014: Remote Sensing Systems AQUA AMSR-E Monthly Environmental Suite on 0.25° grid, version 7.0. Remote Sensing Systems, Santa Rosa, CA. [Available online at www.remss.com/missions/amsre.]

Xie, S.-P., 2004: Satellite observations of cool ocean–atmosphere interaction. *Bull. Amer. Meteor. Soc.*, **85**, 195–208, doi:10.1175/BAMS-85-2-195.

Yasuda, I., 2003: Hydrographic structure and variability in the Kuroshio–Oyashio transition area. *J. Oceanogr.*, **59**, 389–402, doi:10.1023/A:1025580313836.

Yu, L., X. Jin, and R. A. Weller, 2008: Multidecade global flux datasets from the Objectively Analyzed Air–Sea Fluxes (OAFlux) project: Latent and sensible heat fluxes, ocean evaporation, and related surface meteorological variables. Woods Hole Oceanographic Institution OAFlux Project Tech. Rep. OA-2008-01, 64 pp. [Available online at http://oaflux.whoi.edu/pdfs/OAFlux_TechReport_3rd_release.pdf.]